

Observational Insights into Atmospheric CO₂ and CO at the Urban Canopy Layer Top in Metropolitan Shanghai, China

Shuang Fu,^{1, 2} Xuemei Qing,³ Kunpeng Zang,^{1, 3} Yi Lin,^{1, 3} Shuo Liu,^{1, 3} Yuanyuan Chen,^{1, 3} Bingjiang Chen,^{1, 3} Wei Gao,⁴ Martin Steinbacher,⁵ Shuangxi Fang^{1, 3, 6*}

5 ¹Zhejiang Carbon Neutral Innovation Institute & Zhejiang International Cooperation Base for Science and Technology on Carbon Emission Reduction and Monitoring, Zhejiang University of Technology, Hangzhou, China

²State Key Laboratory of Green Chemical Synthesis and Conversion, Zhejiang University of Technology, Hangzhou, China

³College of Environment, Zhejiang University of Technology, Hangzhou, China

⁴Yangtze River Delta Center for Environmental Meteorology Prediction and Warning, Shanghai, China

10 ⁵Laboratory for Air Pollution / Environmental Technology, Empa, 8600 Dübendorf, Switzerland

⁶Collaborative Innovation Center on Forecast and Evaluation of Meteorological Disasters (CIC-FEMD), Nanjing University of Information Science & Technology, Nanjing, China

*Correspondence to: Shuangxi Fang (fangsx@zjut.edu.cn)

Abstract. Major metropolitan areas are critical carbon emission hotspots, and understanding their carbon dynamics is essential
15 for developing targeted climate mitigation strategies. Remote background stations often capture spatially smoothed anthropogenic signals, failing to resolve distinct urban source–sink processes. Here, we leveraged the unique 632-m Shanghai Tower (121.51°E, 31.23°N) to conduct a nearly 2-yr field campaign (April 2021–March 2023), aiming to investigate CO₂ and CO dynamic from the top of urban canopy layer (UCL) via stationary, continuous, single-level, high-precision, in-situ measurements with a cavity ringdown laser spectrometer. Campaign-averaged mole fractions substantially exceeded global
20 and regional backgrounds, confirming a pronounced urban carbon burden. Through a multi-stage filtering framework targeting nocturnal measurements, we derived robust regional background values. Component analysis of CO₂ excess, using CO as a reliable regional combustion tracer, revealed burning of fossil fuels as the dominant contributor (avg. 85%), alongside biogenic processes that enhanced this atmospheric excess, especially in winter under respiratory predominance, but less so in summer when partially offset by net photosynthetic uptake and cleaner air mass dilution. The 2022 Shanghai lockdown provided a
25 natural experiment that underscored the pronounced sensitivity of UCL-top observations to metropolitan-scale anthropogenic perturbations, as reflected in synchronized decline and rapid rebound of CO₂ and CO, along with a marked reversal of their emission ratio compared to 2021. Overall, these findings affirm that UCL-top observations effectively capture integrated metropolitan carbon signals, supporting refined emission tracking and top-down carbon neutrality strategies.

Short Summary. Urban carbon dynamics are critical for climate action, yet remote background monitoring often misses key
30 details. This study utilized the unique vantage point of the 632-m Shanghai Tower to investigate carbon dioxide and carbon monoxide dynamics directly above the urban core. Our research confirms such elevated observations can effectively track metropolitan-scale footprint, revealing fossil fuels as the dominant source (85%) of excess carbon dioxide and supporting targeted reduction measures.

1 Introduction

35 Carbon dioxide (CO₂) is the predominant greenhouse gas (GHG) and a central focus of climate change (Rogelj et al., 2013; Zhu et al., 2019), accounting for the largest share of effective radiative forcing from all long-lived GHGs (2.29 W m⁻², or 66% of the total; AGGI, 2024). The ever-increasing worldwide reliance on fossil fuels has raised atmospheric CO₂ concentrations from a pre-industrial value of 280 ppm to a historic high of 423.9 ppm in 2024 (Fu et al., 2022; Friedlingstein et al., 2022; WMO, 2025), far exceeding the proposed safe threshold of 350 ppm (Rogelj et al., 2013). Carbon monoxide (CO), beyond its
40 direct adverse effects as an atmospheric pollutant on human health and the environment (Henry et al., 2006), acts as an indirect GHG that plays a vital role in atmospheric chemistry by serving as a major sink of tropospheric hydroxyl radicals (OH) (Lelieveld et al., 2016). The OH-initiated reactions that promote CO-to-CO₂ conversion and tropospheric O₃ yield (under sufficient NO_x conditions) competitively deplete atmospheric OH reservoir (Crutzen, 1973; Seinfeld and Pandis, 2016), and thereby prolong the lifetime of other reducing agents, including important GHGs such as methane (CH₄), leading to an indirect
45 positive radiative forcing of 0.2 W m⁻² (Forster et al., 2007; IPCC, 2023). In the recent decade, the global average mole fraction of carbon monoxide (CO) was around 90 ppb (WDCGG, 2025a) with recorded levels between 85 and 200 ppb at background stations in East-Asia (Patel et al., 2024). The efficacy of CO and CO₂ as co-tracers in pinpointing combustion sources and atmospheric processes (Bond et al., 2004; Kamal et al., 2024) necessitates an in-depth investigation into their concurrent footprint patterns and underlying drivers, particularly in regions with high fuel demand and a stringent clean-air imperative.

50 As the world's largest GHG emitter, with cities accounting for a large share of direct carbon emissions (Tong et al., 2018; Meng et al., 2025), China is under mounting international scrutiny in light of its commitment to achieve carbon neutrality by 2060. Supporting this goal, China has been deploying an extensive urban and suburban carbon monitoring network (comprising over 100 stations across more than 30 cities) to complement its WMO/GAW-affiliated background stations, namely one global background station (Waliguan, WLG) and seven regional background stations (WDCGG, 2025b). Although these background
55 stations are primarily located in remote areas, a direct outcome from this monitoring infrastructure is that the data tend to represent blended, regionally-smoothed signals that are often contaminated by ground-based influences (Fang et al., 2015b; Liu et al., 2019; Chen et al., 2024). To extract regionally representative data with minimal local emission influence, a variety of filtering methods have been developed. These range from simple statistical thresholds (e.g., the 1st or 5th percentiles) (Wang et al., 2010; Ye et al., 2024) to more principled approaches including the Robust Extraction of Baseline Signal (REBS)
60 (Ruckstuhl et al., 2012) and Standard Deviation of Running Mean (SDM) (Tsutsumi et al., 2006), diurnal patterns (Yuan et al., 2018), meteorological filtering (MET) (Fang et al., 2014), and the use of specialized tracers such as CO (Tsutsumi et al., 2006; Wang et al., 2010), black carbon (Pu et al., 2014), radon-related (Brunke et al., 2004), and CH₄ (Fang et al., 2015b) for filtering CO₂, which are described in detail on previous publications (Fang et al., 2015b; Liu et al., 2019). Nevertheless, it can be inferred from these limitations that even after filtering, background data from the lower atmosphere remain compromised
65 by near-surface interference, while those from suburban mountaintops are likewise affected by plant canopy dynamics, both of which can consequently obscure real anthropogenic source-sink signals. Furthermore, it is imperative to move beyond

solely quantifying background levels and decipher underlying source–sink dynamics. This expanded focus contributes to a robust, top-down understanding that underpins targeted carbon control strategies, particularly in advanced metropolitan areas with strategically deployed observational infrastructure.

70 The flow over urban areas within the planetary boundary layer (i.e., the urban boundary layer, UBL) is intensified by the urban heat island effect, generating a heat dome that deepens the boundary layer, enhances turbulence mixing, and complicates wind patterns compared to rural surroundings (Oke, 1976; Cosgrove and Berkelhammer, 2018). Conceptually, the UBL consists of several dynamical sublayers (Wang et al., 2014; Vega et al., 2019): the urban canopy layer (UCL), characterized by highly complex flows governed by the geometry of building and vegetation canopies; the roughness sublayer (RSL), a
75 transitional zone extending 2–5 times the mean building height (H_b ; Arnfield, 2003), in which turbulence develops and progressively homogenizes the flow; the surface layer (SL), with nearly constant fluxes and logarithmic wind profile; and the mixed layer, where fluxes and scalars exhibit vertical uniformity. Conventional near-surface observations, typically conducted within the lower UCL, struggle to represent city-scale emissions due to strong hyperlocal influences. In contrast, the world's tallest towers far exceed H_b and allow access to the UCL top and even penetrate the overlying RSL. Thus, stationary
80 measurements are possible at an elevation less affected by transient, hyperlocal sources (e.g., a single vehicle), yet still sensitive to the integrated urban anthropogenic footprint. Although such elevated sites hold promise for capturing metropolitan-scale GHG signals and bridging the gap between ground sources and regional background, their deployment on super-tall skyscrapers remains limited globally.

Shanghai, the largest metropolitan representative in the Yangtze River Delta (YRD) region, China, covers 6,340.5 square
85 kilometers with a permanent population of 24.9 million and total GDP of 4.32 trillion RMB in 2021, making it a carbon emission hotspot (Fig. 1a). This study utilizes the unique Shanghai Tower site (SHT; Figure 1b), a 632-m skyscraper-based platform situated at the UCL top in Shanghai's Lujiazui financial district, to investigate CO₂ and CO dynamics in a megacity environment through a nearly 2-yr continuous campaign (April 2021–March 2023). Through a combination of multi-scale analytical approaches, including robust background filtering and the use of CO as a tracer for fossil-derived CO₂, we quantify
90 the urban carbon burden and identify its key drivers. Moreover, this study capitalizes on the unprecedented natural experiment created by the COVID-19 lockdown and subsequent recovery period in Shanghai to examine the environmental implications of drastic changes in human activity on urban carbon loadings and combustion efficiency. In general, by elucidating the characteristics, composition, and dominant factors governing CO₂ and CO levels from this strategic vantage point directly over the urban core, this study aims to provide several scientific insights that inform targeted carbon mitigation in megacities across
95 China and other rapidly urbanizing regions worldwide.

2 Data and methodology

2.1 Locations and field observations

Continuous in-situ CO₂ and CO measurements were conducted from 17 April 2021 to 6 March 2023 (a period of nearly two years) at the Shanghai Tower (SHT, 121.51°E, 31.23°N), an urban GHG monitoring site erected atop the world's second-tallest skyscraper. The sampling inlet was positioned at 632.0 m above ground level (a.g.l.); with the tower base at 5 m above mean sea level (a.s.l.), this corresponds to approximately 637 m a.s.l. This campaign yielded high-precision, in-situ data on CO₂ and CO levels at the UCL top in metropolitan Shanghai, a key carbon emission hotspot in China (Fig. 1a). As shown in Fig. 1b, the site is situated within the densely urbanized Lujiazui Financial and Commercial District, where it is encircled by roads and high-rise buildings and lies adjacent to the Huangpu River, Shanghai's most vital and busiest shipping artery, thereby being significantly affected by human activities.

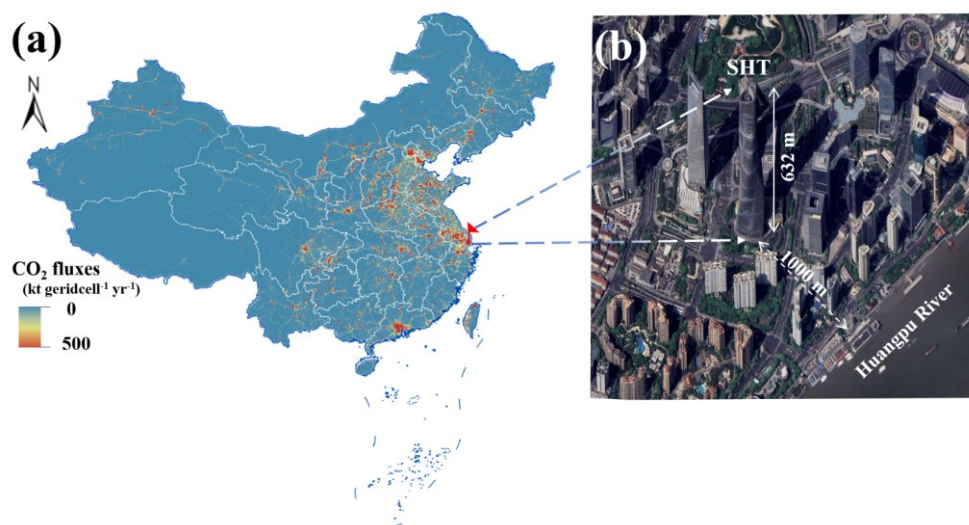


Figure 1: Location and terrain of Shanghai Tower (SHT) site. (a) CO₂ fluxes in 2021 were extracted from Emissions Database for Global Atmospheric Research (EDGAR, <https://edgar.jrc.ec.europa.eu/>). (b) Surrounding area of the SHT site (source: © Google Maps 2025).

2.1.1 CO₂ and CO Field Campaigns

The SHT-based field campaign for CO₂ and CO observation employed stationary, continuous, single-level, high-precision, in-situ measurements via an analytical system equipped with Wave Scan Cavity Ring-down Spectroscopy (WS-CRDS) analyzer (G2401; Picarro Inc., Santa Clara, CA, USA), following a methodology analogous to that described by Fang et al. (2013, 2015a) and implemented in Chen et al. (2024). During this observation, air samples were drawn using a vacuum pump (N022, KNF Neuberger, Germany), with the sampling inlet extending from a 4-m² platform on the tower's uppermost accessible floor (132nd) up to the full structural summit of the Shanghai Tower at 632 m a.g.l. (corresponding to 637 m a.s.l.). This elevation is significantly higher than the highest observation deck open to the public (118th floor, ~ 550 m a.s.l.), and therefore immediate anthropogenic interference there can be considered negligible. The sample stream first passed through a three-stage self-

assembled filter to remove particulate matter, and was then delivered to a glass trap immersed in a methanol bath at $-50\text{ }^{\circ}\text{C}$ (Xiong et al., 2022), where it was dried to a dew point of approximately $-35\text{ }^{\circ}\text{C}$ to reduce the influence of water vapor, followed by temperature equilibration and pressure adjustment prior to analysis. Therefore, the measurements on atmospheric CO_2 and CO were their mole fractions in dry air, and specific calibration procedures are detailed in a previous study (Fang et al., 2014). In brief, the instrument was calibrated daily using two standard gases with high and low concentrations (WH and WL) to establish a two-point linear calibration, while system performance was checked every 6 hours using a target gas (T) with a known concentration. All standards used in the campaign are linked to the WMO- CO_2 _X2019 scale for CO_2 and WMO- CO _X2014A scale for CO . Accounting for a ~ 1 min stabilization period after flushing the internal volume (Fang et al., 2016), an average over the subsequent stable 4-min interval was used for instrument calibration. The measurement precision (1σ over 5 min) derived from repeated target gas measurements was approximately 0.06 ppm for CO_2 and 1.0 ppb for CO during the observation period (Fig. S1), with accuracy meeting WMO/GAW compatibility goals (GGMT, 2024). For clarity in presentation, data were subsequently processed into 10-min or 1-h averages (see Figs. 2 and 3). In addition, comparative observations were conducted simultaneously from April 2021 to December 2022 at a high-altitude background site (Damingshan, DMS, 119.00°E , 30.01°N ; 1489.9 m a.s.l.) in the YRD region, where the measurement and quality control protocols for CO and CO_2 mole fractions were consistent with those at the SHT site.

2.1.2 Additional Environmental Data

Ground-based supplementary measurements, synchronized with the SHT-based observation periods, were obtained from two stations in Shanghai: (i) China's air quality monitoring station of Baoshan Miaohang (BSMH; 121.43°E , 31.33°N ; 12–15 m a.g.l.; 5.6 km from SHT), which provided criteria gaseous pollutants (NO_2 , SO_2 , CO , and O_3 ; 1-h intervals) measured by a series of Thermo Scientific instruments (42i, 43i, 48i, and 49i, respectively); and (ii) the Baoshan Meteorological Station (BS; 31.23°N , 121.29°E ; 1.5 m a.g.l.; 20.9 km from SHT), where meteorological parameters were recorded at 3-h intervals (temperature, pressure, wind direction (wd), wind speed (ws)) and 6-h intervals (cumulative rainfall), as displayed in Supplementary Fig. S1. Additionally, reanalysis data of the planetary boundary layer height (PBLH) at the SHT site were derived from the European Center for Medium-Range Weather Forecasts (ECMWF, 2024). For detailed data sources and dataset, refer to “Data Availability” section.

2.2 Model simulation and apportionment

Considering the high wind speeds (ca. 11.5 m s^{-1}) at the SHT top (637 m a.s.l.) and the aerodynamic effects of its 120° spiral facade (Zhao et al., 2011), the measurement point can be reasonably inferred to lie near the urban roughness sublayer (RSL), where turbulence initiates the homogenization of urban flow. For determining background CO_2 and CO level ($[\text{CO}_2, \text{bk}]$ and $[\text{CO}_{\text{bk}}]$), previous studies have employed tracer analysis related to the 5% lower value of CO (Wang et al., 2010), or data screening focused on intense vertical mixing around noon, (e.g., 10:00–16:00 local time; Fang et al. (2017, 2022)). However, during this campaign, noontime tower-top measurements may be subject to the upward transport of local anthropogenic

150 emissions (see details in Sect. 3.2), as suggested by the PBLH variations (daytime: 728 ± 389 m; nighttime: 290 ± 222 m vs. SHT Top of 637 m; Fig. 2). Thus, to derive regional $\text{CO}_{2, \text{bk}}$ and CO_{bk} amplitudes, we preferentially selected stable nocturnal hours (22:00–05:00 local time) during which the sampling height (SHT top) remained above the urban boundary layer. The procedure for excluding data influenced by local emissions or advected pollution is detailed in Sect. 3.3. The excess CO_2 concentration relative to its background level, expressed as $[\text{CO}_{2, \text{ex}}]$, can be further decomposed as follows:

$$155 \quad [\text{CO}_2] = [\text{CO}_{2, \text{bk}}] + [\text{CO}_{2, \text{ex}}] \\ = [\text{CO}_{2, \text{bk}}] + [\text{CO}_{2, \text{ff}}] + [\text{CO}_{2, \text{bio-dominated}}] + T_{\text{H}} + T_{\text{V}}, \quad (1)$$

Where $[\text{CO}_2]$ is the measured dry-air CO_2 mole fraction (ppm); $[\text{CO}_{2, \text{bk}}]$ represents the background CO_2 level determined by the filtering method (Sect. 3.3); $[\text{CO}_{2, \text{ff}}]$ denotes the CO_2 increment attributed to fossil fuel combustion; and $[\text{CO}_{2, \text{bio-dominated}}]$ is the increment dominated by biological processes (positive for net respiration, negative for net photosynthesis). T_{H} and T_{V} stand for the residual influences of horizontal and vertical transport impacts on the observed CO_2 level, respectively. In practice, the $\text{CO}_{2, \text{bio-dominated}}$ term may partially encompass effects attributed to T_{H} and T_{V} .

To understand the probable transport pathways of air masses arriving at the SHT site, we analyzed back trajectories using the Hybrid Single-Particle Lagrangian Integrated Trajectory (HYSPPLIT) dispersion model from the National Oceanic and Atmospheric Administration Air Resources Laboratory (NOAA ARL). The calculations were based on gridded meteorological data from the Global Data Assimilation System (GDAS) provided by the National Centers for Environmental Prediction (NCEP). Specifically, MeteoInfo software (version 3.3.12) combined with NCEP/GDAS reanalysis data (ftp://arlftp.arlhq.noaa.gov/pub/archives/gdas1, $1^\circ \times 1^\circ$; Rousseau et al., 2004) was used to calculate 72-h back trajectories with 1-h intervals. Trajectories for each season were computed with an arrival height of 600 m a.g.l., corresponding closely to the sampling inlet height at the SHT site. The spatial source distributions of CO_2 and CO were then analyzed using Potential Source Contribution Function (PSCF) method. This method identifies potential source areas by calculating the conditional probability that a measured concentration exceeds a predefined threshold (e.g., the seasonal mean; see Table S1) when an air mass resides over a particular grid cell (Polissar et al., 1999). In the PSCF model, the geographical area covered by the trajectory was divided into grid cells with a spatial resolution of $0.5^\circ \times 0.5^\circ$. The PSCF value for a given cell (i, j) is defined as:

$$175 \quad \text{PSCF}_{ij} = m_{ij}/n_{ij}, \quad (2)$$

Where n_{ij} represented the number of trajectories endpoints passing through the ij unit, and m_{ij} represented the number of trajectories endpoints causing atmospheric CO_2 and CO values to exceed the threshold.

To reduce the influence of n_{ij} outliers, a weight function W_{ij} was applied to obtain a weighted PSCF (WPSCF):

$$W_{ij} = \begin{cases} 1.00 & n_{ij} > 80, \\ 0.70 & 20 < n_{ij} \leq 80, \\ 0.42 & 10 < n_{ij} \leq 20, \\ 0.05 & n_{ij} \leq 10. \end{cases} \quad (3)$$

180 Additionally, to evaluate the influence of local surface wind on species concentrations, we employed the polarPlot function from the OpenAir package in R (Carslaw and Ropkins, 2012; Carslaw, 2015), which uses smoothing techniques to generate bivariate polar plots, depicting pollutant concentration as a continuous surface over ws and wd. The conditional probability function (CPF) was also applied to identify specific wind sectors with a high probability of being associated with elevated concentrations.

185 **3 Results and Discussion**

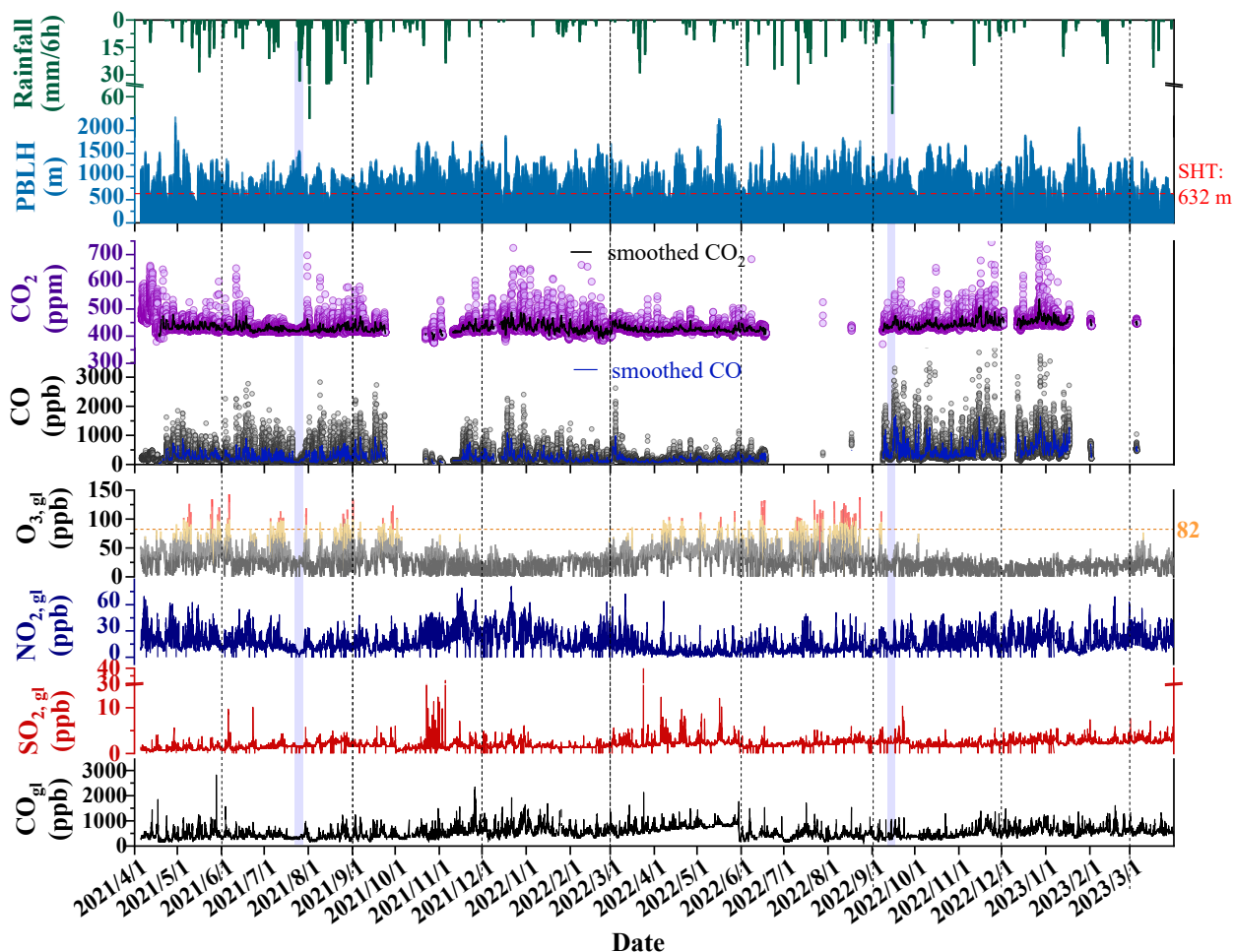
3.1 Overview of the Observations

[Figure 2](#) displays the time series of CO₂ and CO mole fractions measured at the SHT top, alongside ground-level measurements of O₃, NO₂, SO₂, and CO_{gl} (from the nearby BSMH station) and simultaneous records of rainfall (at BS station) and PBLH (reanalysis data) over the 2-yr campaign from April 2021 to March 2023. Additional meteorological parameters, including
190 surface wind, atmospheric pressure, temperature, and dew point, are presented in [Fig. S2](#). Throughout the campaign, CO₂ mole fractions exhibited significant variability, with the 5-min records changing in the range of 362.1–783.7 ppm (388.3–536.5 ppm after 1-h smoothing) and campaign-averaged values (\pm 95% CI) of 433.50 ± 0.33 ppm. Meanwhile, tower-based 5-min CO mole fractions varied considerably from 58.7 to more than 4000 ppb (60.0 to approximately 2000 ppb after smoothing), with an overall average of 313.59 ± 4.91 ppb. Focusing on CO₂, a crucial GHG contributor, [Table S1](#) summarizes CO₂ values
195 measured at various observation sites from recent reports and studies. Generally, the CO₂ measurement conducted at the SHT site was significantly higher than that of a comparable elevation (e.g., Akedala: 420.2 ± 1.4 ppm; 563.3 m a.s.l.; KRE: 427.05 ± 0.64 ; 534 m a.s.l) and those recorded at high-altitude stations (including LLN, WLG, MLO, JFJ, ABLECAS, TPB, TOH and DMS: ca. 417–428 ppm; above 1000 m a.s.l.), whether based on mountains or tower platforms that are situated in global/regional background settings, and also substantially exceeded the global average value of 416.8 ± 0.20 ppm (in 2021–2022;
200 [Table S1](#)). Notably, while elevated, the SHT-based CO₂ value remained appreciably lower than those observed at nearby near-ground sites (e.g., ca. 441.6–446.5 ppm at LAN and HZ site, reported by Chen et al. (2024)), where CO₂ levels are strongly influenced by local anthropogenic emissions. Similarly, the CO value at SHT site was also elevated above regional background level (233.4 ± 3.8 ppb at DMS by Lin et al. (2025)) in the YRD region. These results suggest a distinct surplus of both CO₂ and CO at the UCL top in this highly-urbanized megacity, likely stemming from strong local/regional influences and
205 underscoring the need for further investigation.

It is noteworthy that Shanghai experienced contrasting meteorological conditions and anthropogenic lockdowns during the campaign. In 2021, it received exceptionally high precipitation (1228.2 mm during April–December), influenced by typhoons (e.g., Typhoon In-Fa in July (Wang et al., 2023); [Fig. 2](#)), flood seasons, and plum rains; whereas in 2022, it was recorded significantly lower and unevenly distributed rainfall (870.6 mm, a 38-yr low, including Typhoon Muifa in September
210 (Lin et al., 2024)), alongside epidemic-related lockdowns (Sect. 3.5). Interannual variability in CO₂ was modest (430.94 ± 0.19 ppm in 2021 vs. 433.89 ± 0.15 ppm in 2022), whereas CO was markedly lower in 2021 (290.23 ± 1.88 ppb vs. 313.77 ± 2.26

ppb). This contrast intensified during typhoons, which brought strong winds, heavy rainfall, a sharp V-shaped pressure drop, and cooling (Fig. S2). Specifically, under Typhoon In-Fa, CO decreased by 121.76 ppb (a reduction of 53.4%), compared to a decrease of only 4.2 ppm (0.98%) for CO₂; and during Typhoon Muifa, CO dropped by 246.14 ppb (45.5%) vs. 2.9 ppm (0.67%) for CO₂. Concurrently, ground-level reactive species (such as O₃, NO₂, and SO₂; Fig. 2) exhibited scavenging behavior consistent with that of CO. These results underscore that short-term meteorological perturbations exert a much weaker influence on CO₂ than on CO, reflecting their divergent atmospheric lifetimes and chemical reactivity. Beyond meteorological factors, the interannual variability also reflects differences in regional anthropogenic emissions. In 2021, extensive lockdowns across regions upwind of Shanghai—particularly the North China Plain and central China—substantially suppressed anthropogenic mobile source emissions, contributing to a lower background. Given its elevated location, the SHT site was particularly sensitive to this reduction, capturing the long-range transport signal from distant upwind regions more effectively than surface sites. In contrast, by late 2022, following Shanghai’s prolonged citywide lockdown (March–June 2022) and subsequent nationwide relaxation of COVID-19 restrictions, anthropogenic emissions had rebounded. These emission differences, together with the distinct meteorological conditions noted above, shaped the observed pronounced interannual CO pattern at the elevated SHT site.

Unlike the chemically inert CO₂, CO has a relatively short atmospheric lifetime (τ_{CO} , ~1–3 month; Zheng et al., 2019), governed primarily by OH-initiated oxidation; and its sources are dominated by ground incomplete combustion and, to a lesser extent, the oxidation of CH₄ and biogenic hydrocarbons (Ehhalt and Rohrer, 2009; Seiler, 2010). During this campaign, its diurnal cycles observed at the tower top displayed clear non-uniform distributions, also indicative of near-surface influence (further discussed below). To explore local effects, it is necessary to isolate the regional background signal from the tower-top measurements. Prior to that, vertical CO variations between tower top and base provide a practical perspective for assessing near-surface influences, as discussed in Sect. 3.2.



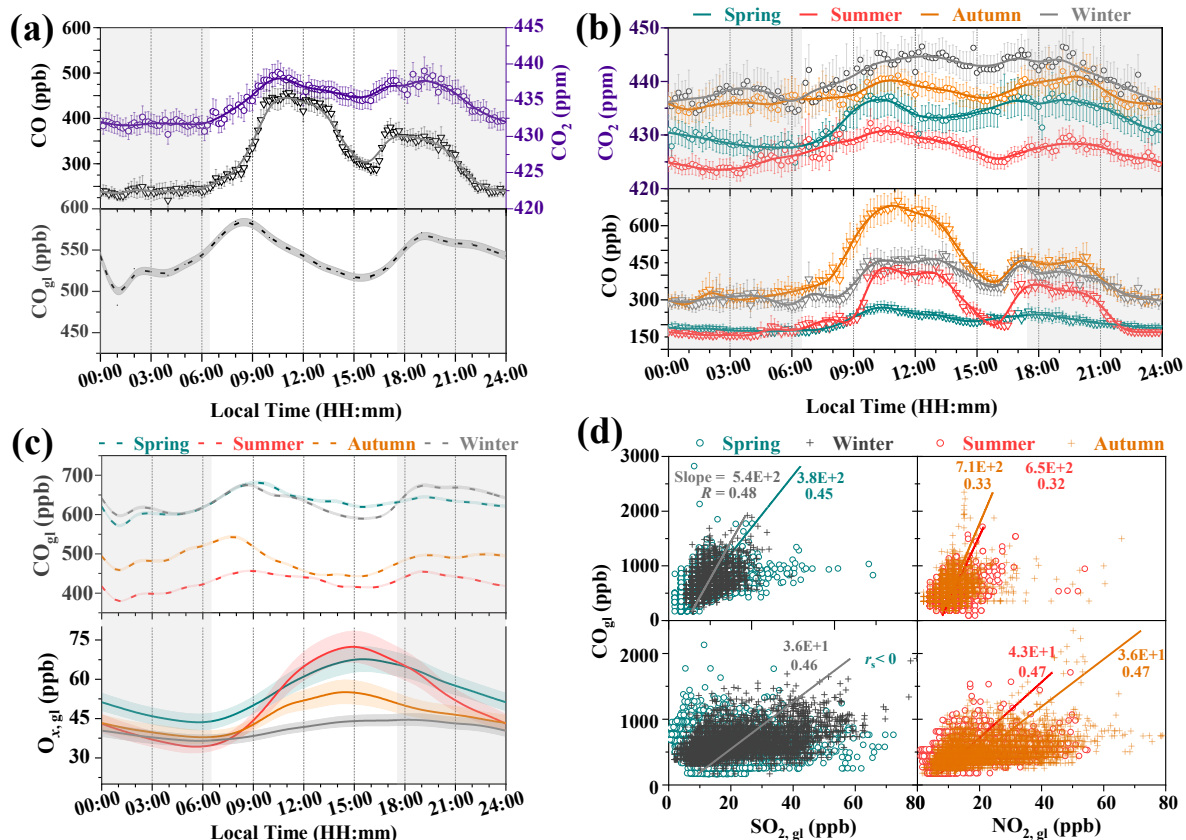
235 **Figure 2: Time series of the key atmospheric species and meteorological parameters during the 2-yr campaign from April 2021 to**
 240 **March 2023.** The presented dataset includes: CO₂ and CO mole fractions measured at the top of Shanghai Tower (SHT; 121.51°E, 31.23°N;
 sampling at 632 m a.g.l.); hourly ground-level gaseous species of O₃, NO₂, SO₂, and CO_{gl} obtained from a nearby ground-based observation
 station (BSMH; 5.6 km from SHT); rainfall data from a separate meteorological station (BSM; 20.9 km from SHT); and hourly reanalyzed
 planetary boundary layer height (PBLH) at the SHT site. The time series of tower-top CO₂ and CO are presented as 10-min averages, with
 smoothed curves generated at 1-h intervals using the curve-fitting method described by Thoning et al. (1989). Pale blue shaded areas indicate
 typhoon events (July 25–26, 2021, and September 14–15, 2022). Intermittent data gaps occurred during the campaign, mainly due to
 logistical disruptions (e.g., standard gas shortages) and restricted site access.

3.2 Temporal Dynamics of Tower-top Measurements Response to Upward Urban plume

245 **Figure 3** illustrates diurnal profiles of tower-top CO and CO₂ alongside ground-level primary pollutants (including CO_{gl})
 throughout the entire campaign and across different seasons. Monthly cycles for species/parameters are provided in **Fig. S3**.
 Both CO₂ and CO exhibited a relatively consistent bimodal pattern, while in terms of CO, its ground mole fraction (avg. 543.11
 ppb) was substantially higher and more variable than that (avg. 313.59 ppb) observed at the tower top. In addition, the initial
 peak at the tower-top occurred around 10:00–11:00 (ca. 443.33 ppb for CO and 438.04 ppm for CO₂), lagging the ground peak

(e.g., ca. 584.71 ppb for CO_{gt}; 8:00–9:00) by about two hours. The UBL uplifts rapidly in the morning, surpassing the SHT top from ca. 9:00–10:00, and remained above it until around 17:00. Accordingly, the intense vertical turbulence during these
250 hours enhanced an upward mixing of gaseous species such as CO, leading to a smaller concentration difference between the tower base and top (CO vs. CO_{gt}), especially on summer and autumn afternoons. In the evening, rush-hour traffic emissions produced a second peak in ground-level CO and tower-top CO₂ at around 19:00, comparable to the morning spikes despite slight declines of 2.3% and 0.2% (Fig. 3a). In contrast, the secondary peak in tower-top CO occurred earlier (~17:00) and was significantly weaker, showing a –19.2% decrease compared to the first one. This pronounced attenuation was likely due to
255 limited replenishment of air masses at the elevated measurement site following the onset of atmospheric subsidence and the PBLH falling below the tower height. At night, CO₂ and CO measurements at the SHT site (UCL top; above urban PBLH, ca. 329.5 ± 246.2 m; Fig. S3) were largely free from ground influence, contrasting with the near-surface accumulation of pollutants in the stable nocturnal layer, a pattern consistent with previous hierarchical tower observations that also recorded limited nighttime concentration variability at upper levels (Denning et al., 2008; Winderlich et al., 2014). This vertical decoupling also
260 aligns with tethered-balloon-based observations, which indicated that the impact of surface emissions on atmospheric carbon was mostly restricted to the lower atmosphere (0–1 km), even to below 300 m (Li et al., 2014; Liu et al., 2025). Consequently, measurements taken at or approaching the PBL top can provide a more representative estimate of regional carbon emission characteristics, and reduce the uncertainty in source rates (Kondo et al., 2006; Wang et al., 2006; Han et al., 2009). However, it is worth noting that, in contrast to the diurnal cycles observed at background tall towers (e.g., KRE; Fig. S4), the SHT-based
265 measurements from an elevated urban core site were subject to pronounced daytime urban emissions, whereas the nighttime data remained more representative of regional surface flux influences. In this context, tower-top nocturnal measurements at SHT site were considered suitable proxies for the regional background, as detailed in Sect. 3.3 alongside the specific filtering criteria.

In addition, Figs. 3a and 3b present diurnal comparisons between tower-top 10-min observations and the unified hourly
270 values. Despite the absence of real-time CO₂ vertical gradient measurements in this campaign, its variation can be inferred to be smaller than that of CO (even in daytime), owing to its chemical stability and high background abundance. The reactive species CO was also analyzed in relation to variations in co-located ground-level pollutants. The unimodal diurnal cycle of odd oxygen (O_x = NO₂ + O₃; Fig. 3c), an index of photochemical oxidation capability (Lin et al., 2021), featured elevated concentrations during daytime photochemical hours that potentially intensified CO depletion, particularly during May–August
275 (Fig. S3). Temporal variations in the correlations between CO and SO₂ (a tracer of coal combustion (Li et al., 2006)) and NO₂ (a byproduct of fuel combustion, particularly traffic-related (Allen et al., 2013)) implied distinct emission regimes (Fig. 3d). In the warmer summer and autumn months, CO showed a stronger correlation with NO₂, underscoring the influence of traffic-related sources. In contrast, the tighter CO–SO₂ association in cold seasons was a possible reflection of sulfur-containing industrial coal combustion. Despite the limited coal combustion and biomass burning for cooking and heating in urban
280 Shanghai, the elevated wintertime concentrations observed in the study region were likely attributable to the widespread use of these fuels in the upwind North China regions (Liu et al., 2016; Zhang et al., 2022).



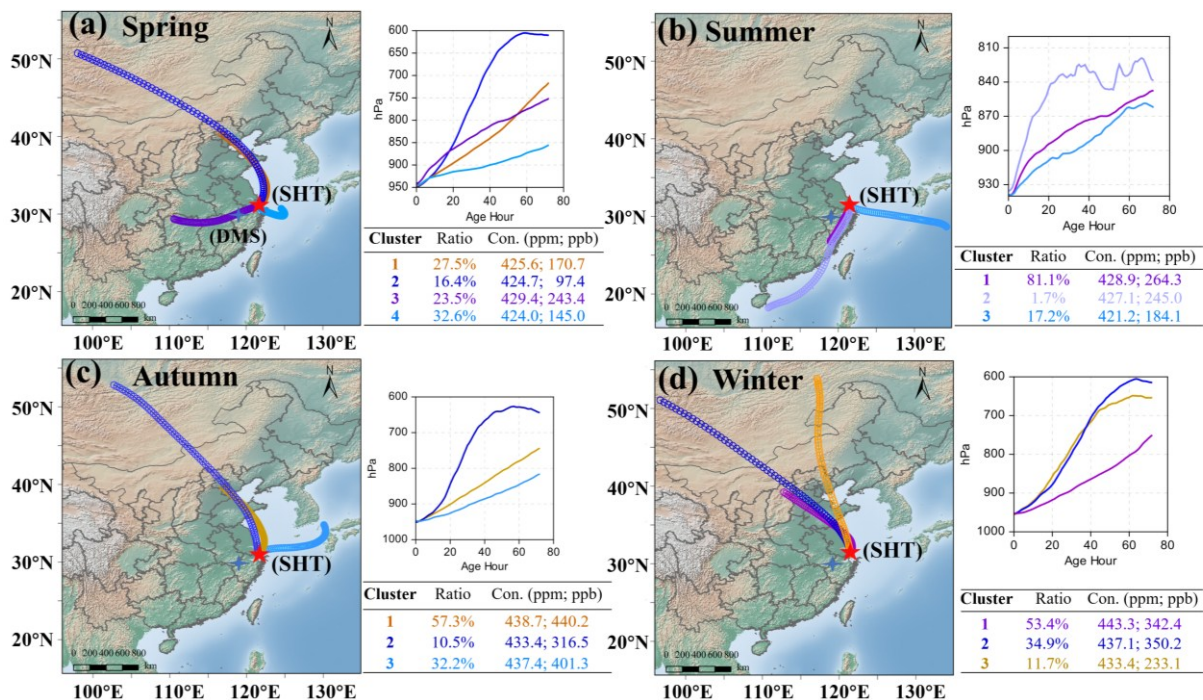
285 **Figure 3: Diurnal profiles of tower-top CO and CO₂ and their relationships with ground-level species across seasons.** Panels (a) and (b) show 10-min average tower-top CO and CO₂ mole fractions with confidence intervals (95% CI) in circles and inverted triangles with error bars. In panels (a–c), the curves with shaded areas display 1-h means and corresponding 95% CI; the unshaded interval in the middle of the day cycle corresponds to daytime, whereas flanking grey shaded periods indicate nighttime (roughly 18:00–06:00, local time). Panel (d) presents the correlations of ground-level primary pollutants (SO₂ and NO₂ vs. CO; d), based on 1-h data.

The observed CO top-base difference (Fig. S5) indicated upward transport (T_V) of an urban plume driven by daytime turbulence, and this effect was potentially reinforced during autumn noontime as high CO levels at the tower top coincided with deeper PBLH, particularly in October (Fig. S3). Moreover, the SHT site appeared to be affected by horizontal transport (T_H) within the lower troposphere (up to 700 hPa), especially from the northwest upwind direction where autumn crop residue burning remains active (Wang et al., 2019), despite the long-standing prohibition of open straw burning in Shanghai (Tian et al., 2022). As an elevated site within a coastal metropolis, SHT is subject to pronounced sea–land breeze circulations, the periodic nature of which significantly complicates pollutant transport and dispersion (Huang et al., 2025). Accordingly, we analyzed 24-h back trajectories from three representative time periods (morning and evening rush hours, and the stable nighttime period; Fig. S6), as well as 72-h trajectories and their associated cluster concentrations (Fig. 4) at the SHT site across seasons. Regarding diurnal cycles, CO₂ and CO levels were primarily influenced by air masses from the eastern coastal areas and by urban plumes passing through the regions of Jiangsu, Anhui, and Zhejiang. In contrast, higher loads of CO and CO₂ at the SHT receptor site in winter were consistently linked to 3-day aged plumes from inland North China, indicating a greater

290

295

300 influence from distant anthropogenic sources driven by land breeze. The sea breeze effect was most pronounced in autumn,
 with the vast majority of air masses arriving at the SHT site within 24 hours being driven by sea breeze (Fig. S6c), broadly
 consistent with recent findings by Huang et al. (2025). Notably, summertime patterns were characterized by a stronger
 influence from sources within the YRD region and by sea breeze extending toward the eastern sea area, accompanied by
 smaller vertical height variations. Furthermore, these anthropogenic impacts were more pronounced on weekdays, as supported
 305 by elevated diurnal concentrations of CO and CO₂ (ca. +5.66 ppb and +1.48 ppm, respectively; Fig. S7) compared to weekends.



310 **Figure 4: Cluster analysis on 72-h back trajectories at the SHT site across different seasons.** The trajectories were computed with an arrival height of 600 m a.g.l., close to the sampling intake height (632 m a.g.l.) at the SHT site. The right panels include cluster-specific pressure profiles and associated CO₂ and CO mole fractions. The SHT and DMS sites in the YRD region are marked as a red five-pointed star and a blue four-pointed star, respectively.

3.3 Background Values Filtering Based on Nighttime Measurements

The principle of background value filtering is to distinguish the signal of a well-mixed atmospheric state from the noise caused by transient emission or sink events. To reduce filtering bias, we applied a meteorological filter to nocturnal tower-top measurements before further statistical processing, as suggested by Ruckstuhl et al. (2012), to derive regional background values of CO and CO₂ (i.e., CO_{bk} and CO_{2, bk}). As noted earlier, the SHT site (637 m a.s.l.) is located at UCL top and typically remains above the nighttime PBLH, experiencing strong winds (~11.5 m s⁻¹) that favor a well-mixed condition. Even so, the measurements could still be affected by certain meteorological conditions and plume transport events, as discussed below.

Rainfall influence: The elevation of nocturnal PBLH during rainfall (ca. +110 m; Fig. 5a) indicated enhanced vertical mixing, likely driven by cloud radiative effects that suppress near-surface cooling, along with mechanical turbulence enhancement and

320 potential evaporative cooling aloft (Paul et al., 2018). Measurements further showed a more pronounced decline in tower-top CO concentrations (-16.9% or -43.0 ppb) than in CO₂ (-0.6% or -2.6 ppm), as compared to stable rain-free nights (22:00–05:00). This distinct nocturnal response can be explained by reduced anthropogenic activity that disproportionately curtails CO emissions but has little effect on persistent CO₂ respiration, coupled with the rainfall-induced downward mixing of cleaner air, to which the locally concentrated CO was significantly more susceptible than the relatively well-mixed CO₂. Therefore, 325 the analysis of concurrent CO_{bk} and CO_{2, bk} (and subsequent parameters) was restricted to non-rainy days, with extreme typhoon events also excluded as previously noted.

Transport impact of upwind, high-load airmass: Pollutant transport also plays a significant role in tower-based measurements, as emphasized earlier. Under the regime of the East Asian monsoon, clean maritime airmasses from the east alternate with polluted air from the west and northwest. These continental inflows were particularly evident in the 330 autumn/winter (Clusters 1 and 2, Fig. 4), leading to a marked increase in CO and CO₂ concentrations. The PSCF-resolved potential source areas (Fig. S8) further identified significant inland extensions during spring, in contrast to a contraction toward the vicinity of the SHT site in other seasons, but it can broadly characterize the overall picture of source influence for the SHT site within a radius of approximately 200 km (with PSCF values > 0.9). In the absence of real-time wind speed and direction data at the tower top, tower-base wind fields were adopted as a proxy, and corresponding distributions of CO and CO₂ across 335 nocturnal (22:00–05:00) and diurnal periods are presented in Figs. 5b and S9, respectively. In particular, a relatively diffuse CO hotspot in the diurnal profile indicated considerable regional transport influence on the SHT receptor site. Under nocturnal conditions, both CO₂ and CO (in terms of averages and top 10% highs) exhibited clustered hotspot patterns in the W, WNW, and NW sectors at ground wind speeds of ca. $1\text{--}4$ m s⁻¹, suggesting persistent and mild upwind transport at night. These western sectors represent the upwind areas where the nighttime offshore land breeze may also partially contribute to the carbon 340 footprint observed at the SHT receptor site (Huang et al., 2025; Zhao et al., 2022).

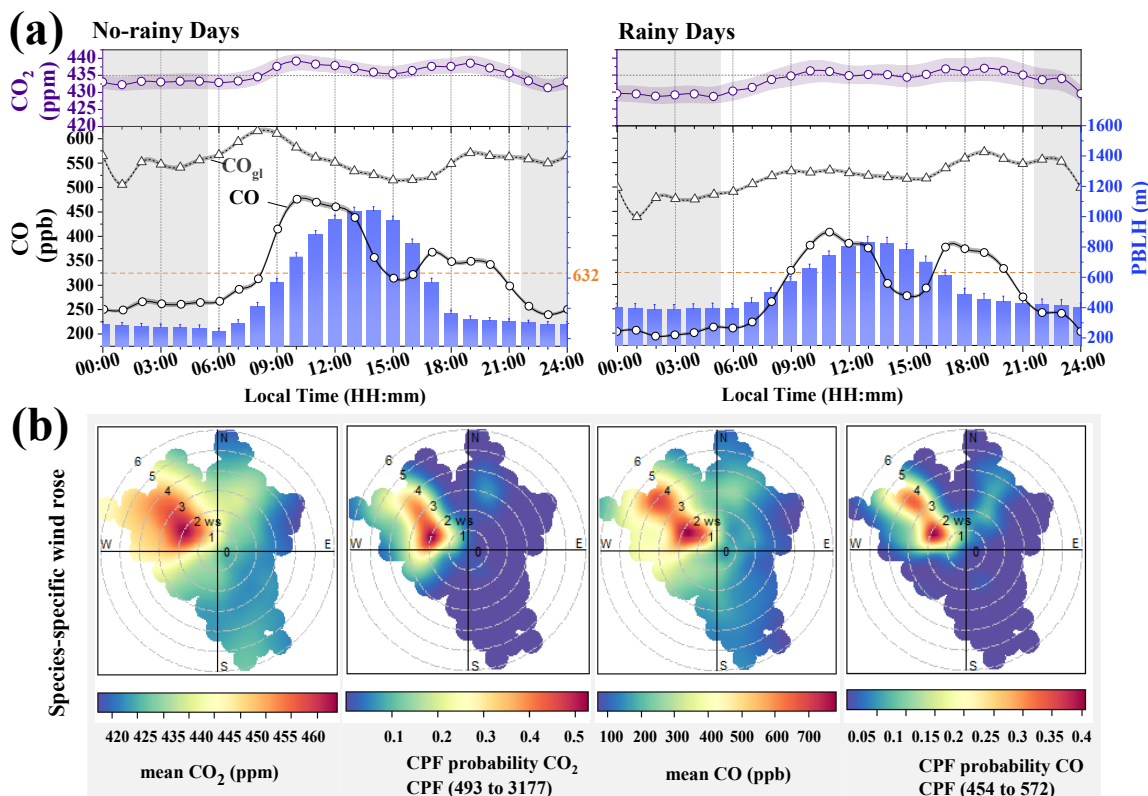
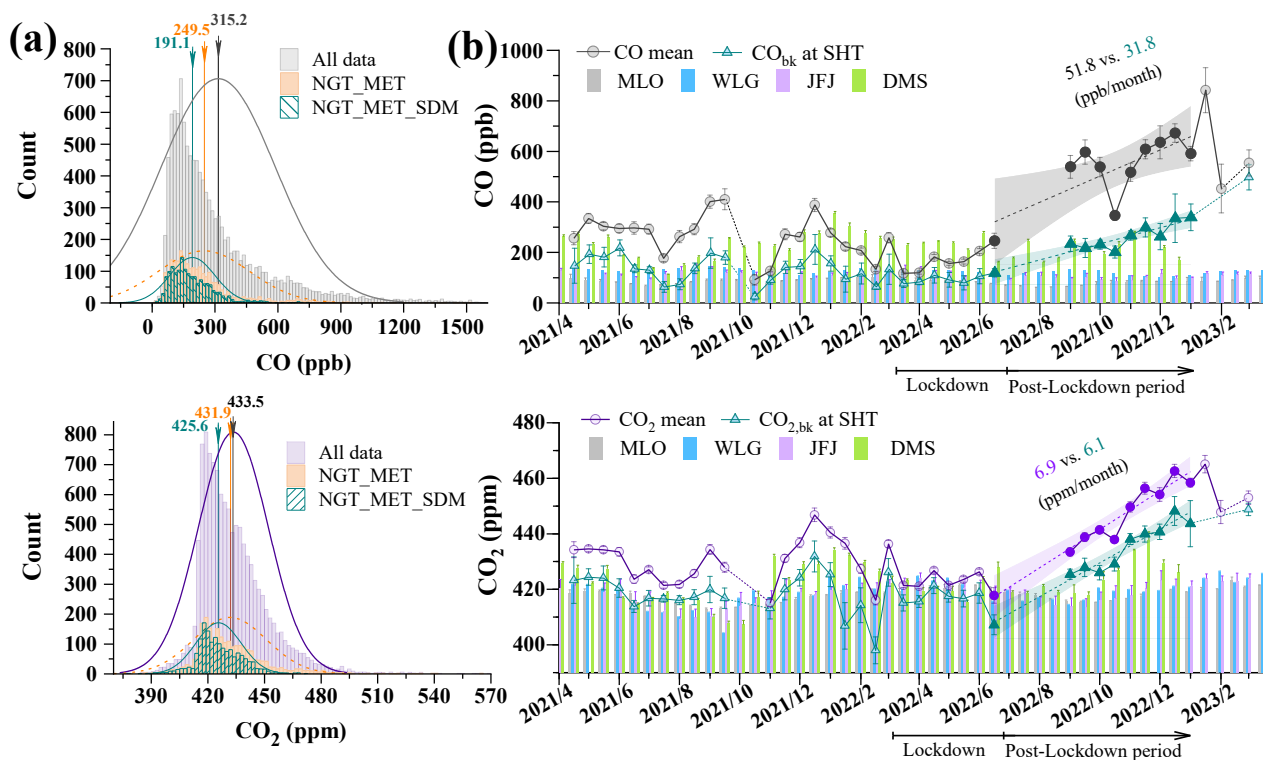


Figure 5: Impacts of rainfall and wind patterns on tower-top CO₂ and CO, alongside associated variations in PBLH and ground-level CO. The darker grey shading area in panels (a) and (b) highlights the condensed stable nighttime period (defined herein as 00:00–05:00 and 22:00–24:00). The Conditional Probability Function (CPF) was applied to the highest 10% of nocturnal CO and CO₂ values in this period to identify potential source directions from the wind rose plots (wind speed, ws, in m s⁻¹).

The selection of regional background data involved a sequential filtering procedure (Fig. 6a). Foremost, the NGT_MET-based process selected concurrent nocturnal CO and CO₂ measurements (22:00–next 5:00 used, constituting 33.3% of the total hourly dataset) from the SHT site, followed by the exclusions of rainy days, typhoon-affected periods, and winds from W, WNW, and NW sectors, which collectively accounted for 14.5% of the total. Subsequently, a comprehensive top-down statistical filter (defined as NGT_MET_SDM and detailed in the following Sect.) was employed to screen out local events (resulting in an additional 5.3% exclusion). Overall, this multi-step filtering process effectively normalized the initially right-skewed distribution of the measurements. The final background dataset consisted of 1,604 hourly records collected over 276 nights during this nearly 2-yr campaign, yielding background concentrations of 425.6 ppm for CO_{2, bk} and 191.1 ppb for CO_{bk}.

Significant short-term variations (e.g., at minute scales) in species concentrations are commonly indicative of local emission or sink processes (Tsutsumi et al., 2006; Seinfeld and Pandis, 2016; Liu et al., 2019). On this basis, we implemented the SDM approach to analyze hourly standard deviation (SD, derived from 5-min resolution data; Fig. S10a) and examined its distribution across the NGT_MET-screened datasets. As shown in Fig. S10b, a high-variability threshold (± 4.4 ppm for CO₂ variation and ± 34 ppb for CO variation over 1-h intervals) was adopted for retracing local events, with 5.1% of records

subsequently flagged as anomalous. Suspected outliers were then re-check and removed (additional ~0.2%) from the
 360 NGT_MET-screened data using two statistical criteria: the conventional $1.5 \times \text{IQR}$ rule ($Q1 - 1.5\text{IQR}$, $Q3 + 1.5\text{IQR}$; Fig. 6a)
 applied to the overall dataset, and the $\pm 3\sigma$ range relative to the smoothed values (Fig. 2) for hourly time series. Following this
 screening procedure, the final dataset comprised 248 sliding daily CO_{bk} and $\text{CO}_{2, \text{bk}}$, each of which satisfied the requirement
 of at least 3 valid nocturnal data within the 8-h period (i.e., 22:00–next 5:00) and served as a dynamic baseline for calculating
 365 subsequent daytime excess concentrations. In cases where no valid background was available for a given day, a biweekly
 sliding average was applied as a substitute to account for temporal variability. Accordingly, Fig. 6b presents CO and CO_2
 levels in semi-monthly intervals during non-rainy periods of the campaign, together with their corresponding background
 values vs. global (MLO, WLG, and JFJ) and YRD regional (DMS) background measurements.



370 **Figure 6: Statistical distributions (panel a) and temporal variations (panel b) of regional background signal at the SHT site via multi-**
stage filtering, compared with synchronous observations from global stations (MLO, WLG, and JFJ) and a regional YRD site (DMS;
 see Table S1 for site details). Monthly-resolution CO data from MLO and WLG, obtained from WDCGG dataset, were linearly interpolated
 to a half-monthly scale. Values are given as mean \pm standard deviation (SD) or mean \pm 95% confidence interval (CI), as specified. For SHT
 and DMS measurements, error bars indicate the 95% CI; for MLO, WLG, and JFJ, error bars indicate SD (source: WDCGG database). The
 375 lockdown (March–June 2022) and post-lockdown (late June 2022–approximately January 2023) periods are marked in panel (b), and growth
 trends during the post-lockdown recovery phase were fitted using the reduced major axis (RMA) method for both overall (solid circles) and
 background (solid triangles) data at SHT.

Regarding CO_{bk} , the filtered mole fractions ($\pm 95\%$ CI: 190.1 ± 4.7 ppb) from tower-top measurements roughly aligned
 with synchronous values recorded at the sites of DMS, MLG, and JFJ (avg. 227.0, 125.2, and 116.6 ppb, respectively; Fig. 6b);

however, this contrasted sharply with surface-based observations, such as the 373–413 ppb range reported at the nearby LAN
 380 site by Liu et al. (2019) using multiple filtering approaches. Given the high spatial heterogeneity of CO in the lower atmosphere
 over non-background regions, the tower-based deployments at the UCL top in this campaign appears to offer a superior vantage
 point for capturing its reliable regional signals. Focusing on $\text{CO}_{2, \text{bk}}$, the derived value at SHT (425.6 ± 0.3 ppm) showed an
 enhancement of approximately 6–7 ppm over the global/regional backgrounds (417.8–422.3 ppm at MLO, WLG, JFJ, and
 DMS; Fig. 6b and Table S1), suggesting significant net source effects within the YRD region, China. The dynamics of
 385 atmospheric CO_2 are governed by multiple factors, including biospheric processes (photosynthesis and respiration), PBLH,
 local anthropogenic activities, etc. (Yang et al., 2021; Chen et al., 2022). Previous studies (Chen et al., 2024; Lin et al., 2025)
 employed filtered DMS data as a background representative for the YRD; however, these data seem to be still confounded by
 sources on or advected to the mountain, with a notably enhanced influence from net vegetative CO_2 release during winter (Fig.
 S11). Specially, nighttime SHT data, measured from within the mixed layer directly above the city center, can be proposed as
 390 a better background proxy. In parallel, anthropogenic emission variations were captured at SHT (Fig. 6b), as shown by
 concurrent declines in CO and CO_2 (including background levels) during the March–June 2022 pandemic lockdown in
 Shanghai and a subsequent rebound during recovery. The strong coherence between CO_2 and CO (a tracer of incomplete
 combustion of carbon-containing fuels (Seiler, 2010)) underscores the significant role of fuel combustion on atmospheric CO_2
 levels. Furthermore, during the recovery period, the total growth rates of CO and CO_2 significantly exceeded their dynamic
 395 regional backgrounds (CO_{bk} and $\text{CO}_{2, \text{bk}}$; Fig. 6b). These growth imbalances can be explained by an increasing concentration
 excess (e.g., $\text{CO}_{2, \text{ex}} = \text{CO}_2 - \text{CO}_{2, \text{bk}}$), highlighting pronounced local net source effects. A detailed compositional analysis of
 these excess signals follows in Sect. 3.4. In addition, a comprehensive case study focusing on Shanghai lockdown and recovery
 phases is presented in Sect. 3.5.

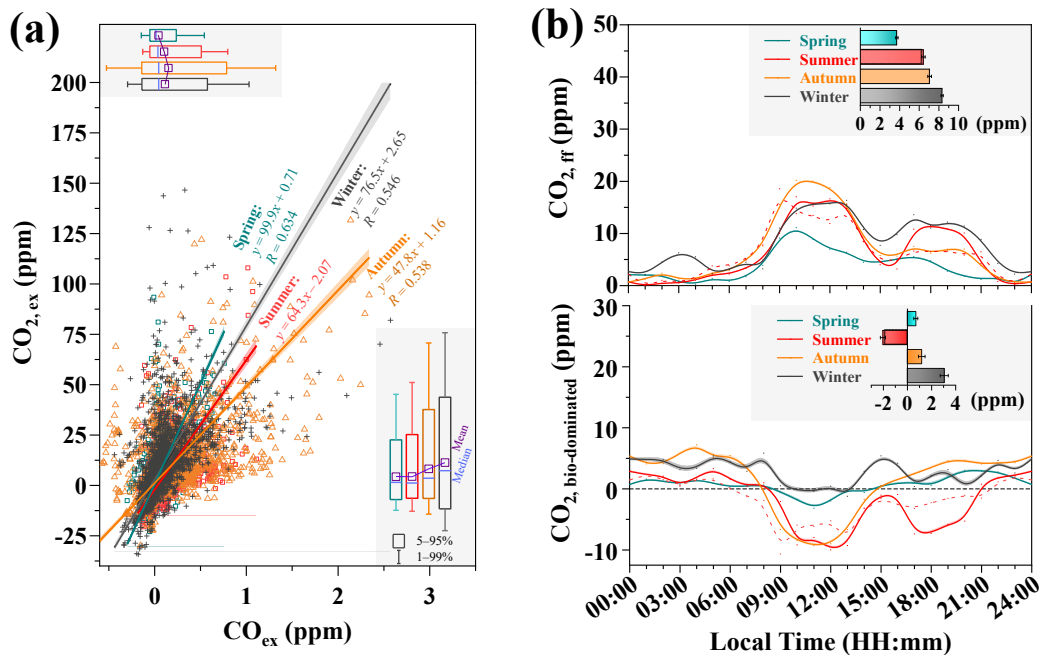
3.4 Analysis on the Main Cause of CO_2 and CO Excesses

400 Specifically, the dynamic excesses of CO and CO_2 (i.e., CO_{ex} and $\text{CO}_{2, \text{ex}}$) were calculated by subtracting the sliding daily
 background values (CO_{bk} and $\text{CO}_{2, \text{bk}}$) from their corresponding real-time measurements. Figure 7 displays the resulting hourly
 excess values and their inter-correlations across seasons. Since CO is mainly co-emitted with CO_2 from fuel combustion
 sources, a significant positive correlation between them is therefore expected when combustion processes dominate the
 observed $\text{CO}_{2, \text{ex}}$. Accordingly, the fossil fuel-derived CO_2 component ($\text{CO}_{2, \text{ff-derived}}$ in Eq. 1) could be quantified using its co-
 405 emission ratio with CO (defined as $k_{\text{CO}_2/\text{CO}}$), as formulated in Eq. (4). It should be noted that $k_{\text{CO}_2/\text{CO}}$ ratios in this study (Fig.
 7a) were determined via the reduced major axis rather than the ordinary least square method to appropriately account for
 uncertainties in both CO_{ex} and $\text{CO}_{2, \text{ex}}$, consistent with previous studies (Hirsch and Gilroy, 1984; Wang et al., 2010).

$$[\text{CO}_{2, \text{ff}}] = ([\text{CO}] - [\text{CO}_{\text{bk}}]) \times k_{\text{CO}_2/\text{CO}} \quad (4)$$

Figure 7a reveals a clear seasonal pattern in $k_{\text{CO}_2/\text{CO}}$ ratios, with higher values in spring (99.9 ppm/ppm) and winter (76.5)
 410 compared to summer (64.3) and autumn (47.8). As mentioned earlier, a lower $k_{\text{CO}_2/\text{CO}}$ ratio in autumn may be related to crop

residue burning as a possible source of autumn CO enhancement (Wang et al., 2019). Moreover, the generally higher $k_{\text{CO}_2/\text{CO}}$ estimates throughout this campaign reflect a lower relative CO ratio (i.e., $k_{\text{CO}/\text{CO}_2}$, $1.5 \pm 0.4\%$) than reported across China (typically 1–6%) (Liu et al., 2018; Xia et al., 2020; Che et al., 2022; Li et al., 2022; Wu et al., 2022), which may be due to relatively well-mixed atmospheric CO levels at the UCL top and/or a gradual improvement in regional combustion efficiency over time. Notably, high-efficiency fossil fuel combustion is typically associated with traffic and power plants (Yang et al., 2020; Che et al., 2022; Zhao et al., 2024). Significant reductions in $k_{\text{CO}/\text{CO}_2}$ have also been observed in specific industrial sectors in the YRD region, such as the steel industry, as suggested by Zhao et al. (2024), and these improvements are largely linked to China's Clean Air Action Plan (2013–2017), after which regional $k_{\text{CO}/\text{CO}_2}$ has stabilized at low levels. Compared with other urban-integrated observations, the derived $k_{\text{CO}/\text{CO}_2}$ at SHT is comparable to values in Sacramento and California (~1%) (Wu et al., 2022), but remains higher than those in Europe areas such as Netherlands (0.2–0.4%; Super et al., 2017) and France (0.3–0.7%; Ammoura et al., 2016; Wu et al., 2022), indicating potential for further decline. This trend was also noticeable under the pandemic-related lockdown, as detailed in Sect. 3.5. Moreover, the relatively weak correlation between summertime $\text{CO}_{2,\text{ex}}$ and CO_{ex} can be explained by disproportionate enhancement of CO_2 signals from biospheric processes (Fig. S3; Wang et al., 2010; Tohjima et al., 2014) and of CO from in-situ oxidation of biogenic hydrocarbons (Bi et al., 2022; Fawole et al., 2022). Despite this, strong vertical mixing during summer helped maintain a good correlation of concurrent CO_2 and CO measurements ($R = 0.53\text{--}0.80$, Fig. S12). In densely populated urban areas, total respiration may substantially contribute to $\text{CO}_{2,\text{ex}}$, forming part of the urban plume. In addition to diel variations in photosynthesis/respiration, atmospheric transport processes (T_{H} and T_{V} ; Eq. 1) may also affect observed $\text{CO}_{2,\text{ex}}\text{--CO}_{\text{ex}}$ correlations. In this study, except for the application of a seasonally constant $k_{\text{CO}_2/\text{CO}}$, we also estimated summertime $\text{CO}_{2,\text{ff}}$ using a time-dependent $k_{\text{CO}_2/\text{CO}}$ expressed as the function of local time (Fig. S13). The results show that $\text{CO}_{2,\text{ff}}$ estimates would decrease by 4–5 ppm in the evening hours (17:00–20:00), while the diurnal average remained nearly unchanged (6.3 vs. 6.4 ppm; Fig. 7b). Consequently, a seasonal $k_{\text{CO}_2/\text{CO}}$ (47.8–99.9; corresponding to $k_{\text{CO}/\text{CO}_2}$ of 0.8–2%) was adopted in the subsequent analysis. Figure 7b further illustrates the diurnal cycles of main $\text{CO}_{2,\text{ex}}$ components ($\text{CO}_{2,\text{ff}}$ and $\text{CO}_{2,\text{bio-dominated}}$) across seasons. In addition, Table S2 summarizes the magnitudes of these resolved excesses relative to filtered background levels.



435

Figure 7: Variations in (panel a): CO₂ and CO excess concentration (i.e., [CO_{2,ex}] and [CO_{ex}]) and (panel b): further apportionment of CO₂ excess to fossil fuel combustion and biologically dominated partition ([CO_{2,ff}] and [CO_{2,bio-dominated}]), respectively. Solid lines: estimates using seasonally constant $k_{CO_2/CO}$ from (a); dashed red line: summer estimates using a time-dependent $k_{CO_2/CO}$.

Overall, the considerable variability in both CO and CO_{bk} at the SHT site (mean CO_{ex} = 98.9 ppb; Table S2), consistent with previous observations (Wang et al., 2010; Liu et al., 2019; Xia et al., 2020), indicates their heightened susceptibility to local/regional, short-term emissions and depletion. It should be noted that our team conducted simultaneous ¹⁴C measurements in atmospheric CO₂ and CO at the site of Hengxiwu (HXW, 119.48°E, 30.60°N; 200 m a.s.l.) in Anji, Zhejiang, a representative area of intensive urbanization in the YRD region. Based on these observations, CO_{2,ff} concentrations were quantified via radiocarbon mass balance (according to Levin et al. (2003) and Vásquez et al. (2022)), and the results (Fig. S14) revealed a strong positive correlation ($R = 0.98$) between CO_{2,ff} and CO_{ex}, with an averaged k_{CO/CO_2} of $1.45 \pm 0.13\%$ that was highly consistent with estimates from the SHT site ($1.5 \pm 0.4\%$). These findings further confirm that CO emissions in the YRD region originate predominantly from fossil fuel combustion and high combustion efficiency there, thereby validating the application of Eq. (4) with an empirically constrained $k_{CO_2/CO}$ for determining regional CO_{2,ff}. Focusing on CO_{2,ex} at SHT site, its averaged concentration was 7.5 ppm, exhibiting a distinct seasonal pattern that peaked in winter (11.4 ppm) and dropped to a minimum in summer and spring (~4.4 ppm). Source decomposition indicated that fossil fuel combustion (CO_{2,ff}) was its dominant source, contributing 6.4 ppm (~85%) to the total excess, with the remainder (1.1 ppm, ~15%) mainly due to biological activities (CO_{2,bio-dominated}). Notably, CO_{2,ff} consistently served as the major source and was the primary driver of CO₂ diurnal cycles (Fig. 3), while CO_{2,bio-dominated} transitioned to a net summertime sink as intense sunlight enhanced photosynthetic CO₂ uptake (Wang et al., 2010; Tohjima et al., 2014). This biological sink offset the apparent effect of ecosystem respiration,

445

450

455 pointing to a potential underestimation of its true role in summer. Moreover, the notable CO_2 , bio-dominated sink (i.e., strong negative values; Fig. 7b) in summer evenings may stem from the oversimplified constant $k_{\text{CO}_2/\text{CO}}$ and/or dilution by advected sea breeze (Fig. 4) from afternoon to evening, observed at the tower top in the evening. Diurnal analysis during winter revealed a slightly amplified CO_2 , bio-dominated signal (3.1 ppm, representing 27% of CO_2 , ex) during non-noon hours, attributable to pronounced net respiration, alongside a substantial CO_2 , ff contribution (8.3 ppm) that increased notably at night (Fig. 7b). The
460 latter half of 2022 coincided with the post-lockdown economic recovery, a period marked by elevated CO_2 and CO levels (Fig. 6b) that were likely linked to combustion-related emissions. The following section aims to investigate the underlying variables responsible for this observed growth.

3.5 Environmental Implications of Lockdown and Recovery Phases

A retrospective look at Shanghai's epidemic measures from late 2019 to early 2023 indicates that this metropolis underwent a
465 phased evolution, commencing with routine containment, pivoting through emergency lockdowns and targeted management, and culminating in a comprehensive reopening. To account for intraseasonal variability, the following analysis focused on monthly comparisons for two specific intervals: the lockdown period (May–Jun 2022 vs. 2021) and post-pandemic recovery period (September 2022–January 2023 vs. the preceding year), as shown in Fig. 8. As reported earlier, lockdown measures primarily curbed residential mobility and public traffic, with limited disruption to industrial operations (SHMS, 2022). Thus,
470 the most prominent change during this campaign was a sharp $56.2 \pm 78.7\%$ drop in traffic-related NO_2 during lockdown, followed by post-lockdown declines of $21.4 \pm 12.2\%$ in NO_2 and $9.4 \pm 4.1\%$ in CO. These variations, against a backdrop of modest PBLH increase ($11.2 \pm 8.4\%$), highlight overall air quality improvement and specific success of curbing vehicle-related emissions (Wang et al., 2022). It should be noted that SO_2 (largely tied to industrial activities) increased significantly during the lockdown, likely due in part to a certain increase in industrial emissions, but driven more by reduced OH regeneration from
475 NO_x decline, which weakened its atmospheric loss (Ye et al., 2023; Zhang et al., 2023). Ground-level CO also exhibited variable patterns (e.g., between May and June, 2021–2022), likely more influenced by localized sources such as residential fuel burning and emissions from emergency services during the pandemic peak than by regional transport.

Generally, UCL top medium- to long-lived carbon oxides (CO and CO_2) showed a pronounced divergence from that of ground-level short-lived pollutants such as NO_x and SO_2 . The ongoing lockdown of about 3–4 months yielded a 38.8% decline
480 in tower-top CO and 1.7% in CO_2 , matching concurrent declines in their regional background and local excess concentrations (-75.4 ± 47.2 and -44.8 ± 9.6 ppb for CO; -2.8 ± 3.5 and -4.4 ± 1.1 ppm for CO_2). In contrast, the subsequent recovery saw a sharp rebound in atmospheric carbon loading, reflected by net increases in both CO (150.2 ± 191.6 and 145.3 ± 142.9 ppb) and CO_2 (15.2 ± 16.4 and 2.9 ± 5.7 ppm) background and excess components. These coordinated variations indicate that anthropogenic activities in this densely-populated metropolis (Shanghai) exerted a dominant influence on the regional carbon
485 footprint and induced an additional localized excess/ deficit. Moreover, the reversal in carbon load differences between the two scenarios implies a fundamental shift in emission structure. This transition is clearly reflected in the combustion efficiency

proxy, $k_{\text{CO}_2/\text{CO}}$, which increased by ~ 25 during the control period before a decrease of 36 ± 22 in the relaxation phase (Fig. 8). A widespread enhancement in $k_{\text{CO}_2/\text{CO}}$ in response to anthropogenic emission controls has been also observed in other conditions, such as its near doubling during the 2008 Beijing Olympics (46.4 ± 4.6) relative to the pre-Olympic period (23–29 in September 2005–2007) (Wang et al., 2010). This trend is further supported by long-term interannual increases, exemplified by a rise from 10–18 to ca. 50 based on $\Delta^{14}\text{C}$ measurements in the Los Angeles basin between 1980 and 2008 (Djuricin et al., 2012), and a climb from 46.5 to about 80–90 over the YRD region from 2012 to 2021 (Wu et al., 2022; Zhao et al., 2024).

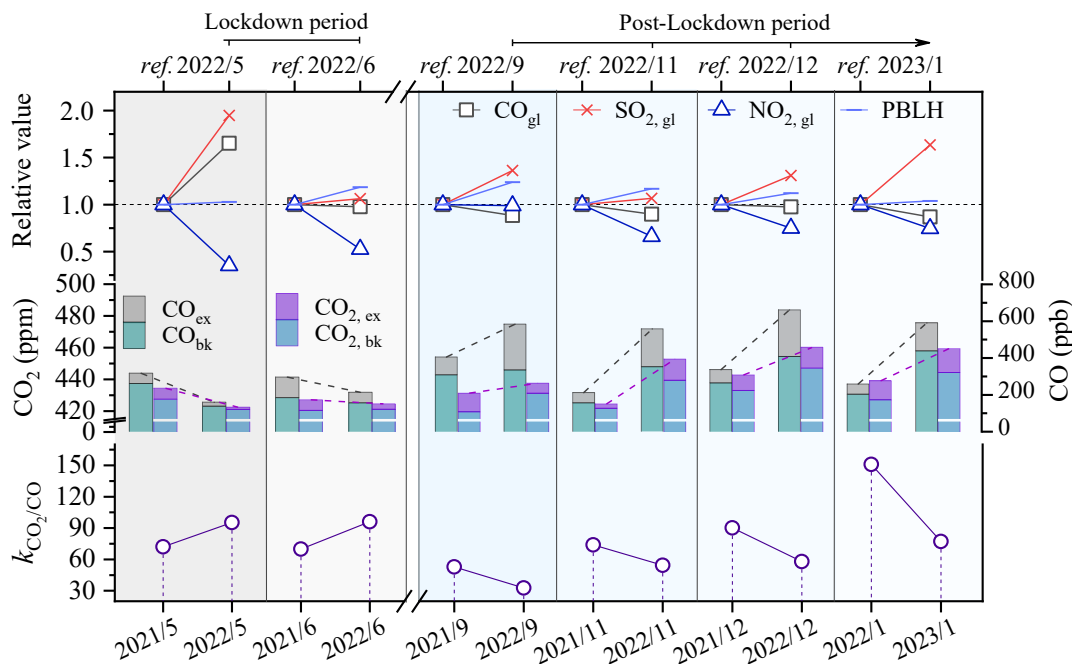


Figure 8: Interannual comparison of ground-level and tower-top species and associated parameters for the lockdown period (May–June 2022 vs. 2021) and post-pandemic recovery period (September 2022–January 2023 vs. 2021–2022).

UCL-top measurements are representative of the vertically integrated and homogenized urban carbon footprint, whereas ground-level observations are strongly influenced by local, transient sources. The 2022 lockdown in Shanghai precipitated a near-total collapse of its urban and intercity transport systems, showing a dramatic plummet of over 90% in aviation, rail, and maritime passenger volumes (MOT, 2022), an approximate 20% decline in road traffic, and a severe operational crisis at the Port of Shanghai with soaring vessel queues and cargo backlogs. The recovery period saw a gradual normalization of port operations, concurrent with a lasting behavioral shift toward private car usage over public transport. Variations in combustion efficiency across fuel types (e.g., gasoline, diesel, and biomass) and traffic states (e.g., moving, congested, or stationary) (Westerdahl et al., 2009; Popa et al., 2014; Wu et al., 2022) are also reflected in the differences of $k_{\text{CO}_2/\text{CO}}$. The observed elevation in $k_{\text{CO}_2/\text{CO}}$ (Fig. 8) during the lockdown may be explained by the sharp reduction in urban traffic, along with a temporarily increased contribution from low- $k_{\text{CO}_2/\text{CO}}$ diesel shipping near the port (Zhang et al., 2016; Kim et al., 2020; Wu et al., 2022). In the recovery phase, the $k_{\text{CO}_2/\text{CO}}$ dropped by 36 ± 22 from ca. 90 ± 22 , and this shift can be attributed to resumption

of gasoline vehicle-related traffic and potentially increasing influence from upwind inefficient combustion sources such as biomass burning Tohjima et al. (2014) in autumn and winter, 2022. Generally, in our year-to-year comparison for the same month (without accounting for biospheric influences here), localized CO₂ excess or deficit could be primarily attributed to variations in emissions related to fossil fuels (CO_{2, ff}).
510

4 Conclusions

This study, based on a nearly 2-yr campaign conducted at the Shanghai Tower (632 m a.g.l.), systematically investigates for the first time the temporal dynamics and drivers of atmospheric CO₂ and CO in metropolitan Shanghai. Elevated concentrations (433.50 ± 0.33 ppm for CO₂ and 313.59 ± 4.91 ppb for CO) at this site revealed excess carbon in the urban atmosphere aloft, with the lagged peak against ground-based CO serving as a clear indicator of daytime upward transport of local anthropogenic emissions. By applying a robust background filtering procedure (NGT_MET_SDM) focused on nocturnal stable periods and combining meteorological and statistical methods, we identified that the CO background level was comparable to, or slightly below, that recorded at the DMS background site in the YRD region. In contrast, the higher CO₂ regional background level combined with significant CO₂ excess over diurnal cycle characterizes this region as a perennial CO₂ hotspot, a characteristic urban phenomenon further intensified by local net source effects in megacities.
515
520

The relationship between CO₂ and CO excess at SHT, corroborated by independent CO₂-Δ¹⁴C and CO correlations from the YRD region, definitively confirms that the region exhibits high fossil fuel combustion efficiency and that CO emissions are overwhelmingly fossil-derived. Accordingly, through excess concentration analysis and CO₂/CO emission ratio ($k_{\text{CO}_2/\text{CO}}$) tracing, we further quantified source contributions: fossil fuel combustion accounted for ~85% (7.5 ppm) of the diurnal CO_{2, ex}, with the remainder dominated by biogenic processes that shifted from a net sink in summer (-2.0 ppm) to a source in winter (+2.8 ppm). Moreover, this campaign successfully captured a clear signature of emission changes during the pandemic lockdown and recovery. A distinct pattern was observed at the tower top, differing somewhat from ground-level measurements, characterized by a simultaneous decline in both CO₂ and CO levels (including their backgrounds) followed by a coordinated rapid rebound. Critically, the year-on-year difference in the $k_{\text{CO}_2/\text{CO}}$ ratio increased during the lockdown and decreased afterwards, indicating a structural shift in dominant emission sources. These findings demonstrate a sensitive response of atmospheric carbon footprint at the urban canopy top to variations in anthropogenic emissions.
525
530

Our findings suggest that utilizing existing infrastructure at the UCL top (or above H_b) minimizes near-ground effects and provides an immediate and representative signal of the metropolitan-scale anthropogenic influence on GHG concentrations in non-background regions. This approach captures the dynamically mixed urban plume, offering insights that may distinct from those obtained at background sites, which are influenced by broader regional conditions. On this basis, we also recommend combining these measurements with complementary platforms (e.g., drones, tethered balloons and remote sensing) to better resolve vertical profiles of GHG within the UBL. Moreover, extending the current excess CO₂ analysis with multi-tracer techniques such as incorporating isotopic or specific VOC markers would enable more precise apportionment of
535

contributions from fossil fuel, biogenic, and industrial sources, thereby reducing attribution uncertainty. Together, these
540 advances will strengthen the scientific basis for evaluating carbon neutrality policies and quantifying impacts of extreme events
such as public health interventions and severe weather on urban GHG dynamics.

Data Availability. The gridded meteorological data utilized were sourced from the NOAA Air Resources Laboratory (NOAA-
ARL, 2024). PBLH data are reanalysis products from the fifth generation ECMWF reanalysis for the global climate and
weather (ERA5, 2025). Global CO₂ measurements from multiple meteorological stations are available from WDCGG (2025b).
545 Air quality observations from China’s national monitoring network are accessible via CNEMC (2025), and meteorological
data are available from CMDC (2024). The data on measured CO₂ and CO profiles in the study are available at Fu and Fang
(2025).

Supplement. The supplement related to this article is available online at: Supporting Information, and in which Tables S1–S2
provide an overview of measured CO₂ mixing ratio across sites and component analysis of CO₂ and CO at the SHT site; Figures
550 S1–S12 mainly present the relevant meteorological parameters, as well as supported profile information on CO₂, CO and their
associated background and excess values.

Author Contributions. SF (Shuangxi Fang) led the study. KZ, XQ, BC, and WG contributed to the instrument calibration and
field measurements. SL and YC contributed to data quality control. SF (Shuang Fu) analyzed the observation data, conducted
the study concept, and wrote the manuscript draft with input from all co-authors. YL and MS were involved in the scientific
555 interpretation and discussions. The paper was reviewed and commented on by all authors.

Competing interests. The authors declare that they have no conflict of interest.

Acknowledgements. This study was financially supported by the National Key Research and Development Program of China
(2023YFC3705205), the “Pioneer” and “Leading Goose” R&D Program of Zhejiang (2024C03246), and National Natural
Science Foundation of China (Grant No. 42275113).

560 **References**

- AGGI: The NOAA annual greenhouse gas index (AGGI), available at: <https://gml.noaa.gov/aggi/aggi.html> (last access: 25
October 2025), 2024.
- Allen, R. W., Gombojav, E., Barkhasragchaa, B., Byambaa, T., Lkhasuren, O., Amram, O., Takaro, T. K., and Janes, C. R.:
An assessment of air pollution and its attributable mortality in Ulaanbaatar, Mongolia, *Air Qual. Atmos. Health*, 6, 137–
565 150, <https://doi.org/10.1007/s11869-011-0154-3>, 2013.
- Ammoura, L., Xueref-Remy, I., Vogel, F., Gros, V., Baudic, A., Bonsang, B., Delmotte, M., Té, Y., and Chevallier, F.:
Exploiting stagnant conditions to derive robust emission ratio estimates for CO₂, CO and volatile organic compounds in
Paris, *Atmos. Chem. Phys.*, 16, 15653–15664, <https://doi.org/10.5194/acp-16-15653-2016>, 2016.
- Arnfield, A. J.: Two decades of urban climate research: a review of turbulence, exchanges of energy and water, and the urban
570 heat island, *Int. J. Climatol.*, 23, 1–26, <https://doi.org/10.1002/joc.859>, 2003.

- Bi, J., Zuidema, C., Clausen, D., Kirwa, K., Young Michael, T., Gasset Amanda, J., Seto Edmund, Y. W., Sampson Paul, D., Larson Timothy, V., Szpiro Adam, A., Sheppard, L., and Kaufman Joel, D.: Within-city variation in ambient carbon monoxide concentrations: Leveraging low-cost monitors in a spatiotemporal modeling framework, *Environ. Health Perspect.*, 130, 097008, <https://doi.org/10.1289/EHP10889>, 2022.
- 575 Bond, T. C., Streets, D. G., Yarber, K. F., Nelson, S. M., Woo, J.-H., and Klimont, Z.: A technology-based global inventory of black and organic carbon emissions from combustion, *J. Geophys. Res.: Atmos.*, 109, <https://doi.org/10.1029/2003JD003697>, 2004.
- Brunke, E. G., Labuschagne, C., Parker, B., Scheel, H. E., and Whittlestone, S.: Baseline air mass selection at Cape Point, South Africa: application of ^{222}Rn and other filter criteria to CO_2 , *Atmos. Environ.*, 38, 5693–5702, <https://doi.org/10.1016/j.atmosenv.2004.04.024>, 2004.
- 580 Carslaw, D. C.: The openair manual — Open-source tools for analysing air pollution data. Manual for version 1.1-4, King's College London, <https://github.com/davidcarlsaw/openair>, 2015.
- Carslaw, D. C. and Ropkins, K.: Openair — An R package for air quality data analysis, *Environ. Modell. Softw.*, 27–28, 52–61, <https://doi.org/10.1016/j.envsoft.2011.09.008>, 2012.
- 585 Che, K., Liu, Y., Cai, Z., Yang, D., Wang, H., Ji, D., Yang, Y., and Wang, P.: Characterization of regional combustion efficiency using ΔXCO : ΔXCO_2 observed by a portable fourier-transform spectrometer at an urban site in Beijing, *Adv. Atmos. Sci.*, 39, 1299–1315, <https://doi.org/10.1007/s00376-022-1247-7>, 2022.
- Chen, Y., Cheng, J., Song, X., Liu, S., Sun, Y., Yu, D., and Fang, S.: Global-scale evaluation of XCO_2 products from GOSAT, OCO-2 and carbontracker using direct comparison and triple collocation method, *Remote Sens.*, 14, <https://doi.org/10.3390/rs14225635>, 2022.
- 590 Chen, Y., Lu, Y., Qi, B., Ma, Q., Zang, K., Lin, Y., Liu, S., Pan, F., Li, S., Guo, P., Chen, L., Lan, W., and Fang, S.: Atmospheric CO_2 in the megacity Hangzhou, China: Urban-suburban differences, sources and impact factors, *Sci. Total Environ.*, 926, <https://doi.org/10.1016/j.scitotenv.2024.171635>, 2024.
- CMDC, China Meteorological Data Service Center: China Meteorological Data [data set], <https://fairsharing.org/10.25504/FAIRsharing.52d9fa>, 2024.
- 595 CNEMC, China National Environmental Monitoring Centre: National Urban Air Quality Real-time Release Platform [data set], <https://air.cnemc.cn:18007/>, 2025.
- CNCA: Carbon Neutral Cities Alliance, available at: <https://carbonneutralcities.org/about/> (last access: 25 October 2025), 2020.
- Cosgrove, A. and Berkelhammer, M.: Downwind footprint of an urban heat island on air and lake temperatures, *npj Clim. Atmos. Sci.*, 1, <https://doi.org/10.1038/s41612-018-0055-3>, 2018.
- 600 Crutzen, P.: A discussion of the chemistry of some minor constituents in the stratosphere and troposphere, *PAGEOPH*, 106–108, 1385–1399, <https://doi.org/10.1007/BF00881092>, 1973.
- Denning, A. Zhang, N., Yi, C., Branson, M., Davis, K., Kleist, J., and Bakwin, P.: Evaluation of modeled atmospheric boundary layer depth at the WLEF tower, *Agric. For. Meteorol.*, 148, 206–215, <https://doi.org/10.1016/j.agrformet.2007.08.012>, 2008.
- 605 Djuricin, S., Xu, X., and Pataki, D. E.: The radiocarbon composition of tree rings as a tracer of local fossil fuel emissions in the Los Angeles basin: 1980–2008, *J. Geophys. Res.: Atmos.*, 117, <https://doi.org/10.1029/2011JD017284>, 2012.
- ERA5, the fifth generation ECMWF reanalysis for the global climate and weather: ERA5 hourly data on single levels from 1940 to present, Copernicus Climate Data Store [data set], <https://doi.org/10.24381/cds.adbb2d47>, 2025

- 610 Ehhalt, D. H. and Rohrer, F.: The tropospheric cycle of H₂: A critical review, *Tellus B: Chem. Phys. Meteorol.*, 61, 500–535, <http://doi.org/10.1111/j.1600-0889.2009.00416.x>, 2009.
- Fang, S., Luan, T., Zhang, G., Wu, Y., and Yu, D.: The determination of regional CO₂ mole fractions at the Longfengshan WMO/GAW station: A comparison of four data filtering approaches, *Atmos. Environ.*, 116, 36–43, <https://doi.org/10.1016/j.atmosenv.2015.05.059>, 2015a.
- 615 Fang, S., Tans, P. P., Steinbacher, M., Zhou, L. X., and Luan, T.: Comparison of the regional CO₂ mole fraction filtering approaches at a WMO/GAW regional station in China, *Atmos. Meas. Tech.*, 8, 5301–5313, <https://doi.org/10.5194/amt-8-5301-2015>, 2015b.
- Fang, S., Zhou, L., Masarie, K. A., Xu, L., and Rella, C. W.: Study of atmospheric CH₄ mole fractions at three WMO/GAW stations in China, *J. Geophys. Res.: Atmos.*, 118, 4874–4886, <https://doi.org/10.1002/jgrd.50284>, 2013.
- 620 Fang, S., Tans, P. P., Steinbacher, M., Zhou, L., Luan, T., and Li, Z.: Observation of atmospheric CO₂ and CO at Shangri-La station: results from the only regional station located at southwestern China, *Tellus B: Chem. Phys. Meteorol.*, 68, <https://doi.org/10.3402/tellusb.v68.28506>, 2016.
- Fang, S., Tans, P. P., Yao, B., Luan, T., Wu, Y., and Yu, D.: Study of atmospheric CO₂ and CH₄ at Longfengshan WMO/GAW regional station: The variations, trends, influence of local sources/sinks, and transport, *Sci. China Earth Sci.*, 60, 1886–
- 625 1895, <https://doi.org/10.1007/s11430-016-9066-3>, 2017.
- Fang, S., Du, R., Qi, B., Ma, Q., Zhang, G., Chen, B., and Li, J.: Variation of carbon dioxide mole fraction at a typical urban area in the Yangtze River Delta, China, *Atmos. Res.*, 265, <https://doi.org/10.1016/j.atmosres.2021.105884>, 2022.
- Fang, S., Zhou, L., Tans, P., Ciais, P., Steinbacher, M., Xu, L., and Luan, T.: In situ measurement of atmospheric CO₂ at the four WMO/GAW stations in China, *Atmos. Chem. Phys.*, 14, 2541–2554, <https://doi.org/10.5194/acp-14-2541-2014>,
- 630 2014.
- Fawole, O. G., Yusuf, N., Sunmonu, L. A., Obafaye, A., Audu, D. K., Onuorah, L., Olusegun, C. F., Deme, A., and Senghor, H.: Impacts of COVID-19 restrictions on regional and local air quality across selected West African cities, *Geohealth*, 6, e2022GH000597, <https://doi.org/10.1029/2022gh000597>, 2022.
- Forster, P., Ramaswamy, V., Artaxo, P., Berntsen, T., Betts, R., Fahey, D., Haywood, J., Lean, J., Lowe, D., Myhre, G.,
- 635 Nganga, J., Prinn, R., Raga, G., Michael, S., and Dorland, R.: The Physical Science Basis of Climate Change: Changes in Atmospheric Constituents and in Radiative Forcing, in, edited by: S. Solomon et al. (eds.), C. U. P., Cambridge, UK, Chapter 2, 2007.
- Friedlingstein, P., Jones, M. W., O'Sullivan, M., Andrew, R. M., Bakker, D. C. E., Hauck, J., Le Quééré, C., Peters, G. P., Peters, W., Pongratz, J., Sitch, S., Canadell, J. G., Ciais, P., Jackson, R. B., Alin, S. R., Anthoni, P., Bates, N. R., Becker, M.,
- 640 Bellouin, N., Bopp, L., Chau, T. T. T., Chevallier, F., Chini, L. P., Cronin, M., Currie, K. I., Decharme, B., Djeutchouang, L. M., Dou, X., Evans, W., Feely, R. A., Feng, L., Gasser, T., Gilfillan, D., Gkritzalis, T., Grassi, G., Gregor, L., Gruber, N., Gürses, Ö., Harris, I., Houghton, R. A., Hurtt, G. C., Iida, Y., Ilyina, T., Luijkx, I. T., Jain, A., Jones, S. D., Kato, E., Kennedy, D., Goldewijk, K. K., Knauer, J., Korsbakken, J. I., Körtzinger, A., Landschützer, P., Lauvset, S. K., Lefèvre, N., Lienert, S., Liu, J., Marland, G., McGuire, P. C., Melton, J. R., Munro, D. R., Nabel, J. E. M. S., Nakaoka, S. I., Niwa, Y., Ono, T., Pierrot, D., Poulter, B., Rehder, G., Resplandy, L., Robertson, E., Rödenbeck, C., Rosan, T. M., Schwinger, J., Schwingshackl, C., Séférian, R., Sutton, A. J., Sweeney, C., Tanhua, T., Tans, P. P., Tian, H., Tilbrook, B., Tubiello, F., Van Der Werf, G. R., Vuichard, N., Wada, C., Wanninkhof, R., Watson, A. J., Willis, D., Wiltshire, A. J., Yuan, W., Yue, C., Yue, X., Zaehle, S., and Zeng, J.: Global Carbon Budget 2021, *Earth Syst. Sci. Data*, 14, 1917–2005, <https://doi.org/10.5194/essd-14-1917-2022>, 2022.
- 645

- 650 Fu, J., Li, P., Lin, Y., Du, H., Liu, H., Zhu, W., and Ren, H.: Fight for carbon neutrality with state-of-the-art negative carbon emission technologies, *Eco-Environ. Health*, 1, 259–279, <https://doi.org/10.1016/j.eehl.2022.11.005>, 2022.
- Fu, S., and Fang, S.: Shanghai Tower atmospheric CO₂ and CO during 2021-2023, figshare [data set], <https://doi.org/10.6084/m9.figshare.30918203>, 2025.
- GGMT: GAW Report No. 292: Twenty-first WMO/IAEA Meeting on Carbon Dioxide, Other Greenhouse Gases and Related Measurement Techniques (GGMT-2022), available at: <https://library.wmo.int/records/item/68925> (last access: 21 November 2025), 2024.
- Han, S., Kondo, Y., Oshima, N., Takegawa, N., Miyazaki, Y., Hu, M., Lin, P., Deng, Z., Zhao, Y., Sugimoto, N., and Wu, Y.: Temporal variations of elemental carbon in Beijing, *J. Geophys. Res.: Atmos.*, 114, <https://doi.org/10.1029/2009JD012027>, 2009.
- 660 Henry, C. R., Satran, D., Lindgren, B., Adkinson, C., Nicholson, C. I., and Henry, T. D.: Myocardial injury and long-term mortality following moderate to severe carbon monoxide poisoning, *JAMA*, 295, 398–402, <https://doi.org/10.1001/jama.295.4.398>, 2006.
- Hirsch, R. and Gilroy, E.: Methods of fitting a straight line to data: Examples in water resources, *Water Resources Bulletin*, 20, 705–711, <https://doi.org/10.1111/j.1752-1688.1984.tb04753.x>, 1984.
- 665 Huang, Y., Li, S., Zhu, Y., Liu, Y., Hong, Y., Chen, X., Deng, W., Xi, X., Lu, X., and Fan, Q.: Increasing sea-land breeze frequencies over coastal areas of China in the past five decades, *Geophys. Res. Lett.*, 52, e2024GL112480, <https://doi.org/10.1029/2024GL112480>, 2025.
- IPCC: Intergovernmental Panel on Climate Change. Climate Change 2021 – The Physical Science Basis: Working Group I Contribution to the Sixth Assessment Report of the Intergovernmental Panel on Climate Change, Cambridge University Press, 675–714 pp., <https://doi.org/10.1017/9781009157896>, 2023.
- 670 Kamal, A. T. M. M., Islam, M. S., Zaman, S. U., Miah, M. J., Ahmed, T., Hoque, S., and Salam, A.: Quantification and source apportionment of atmospheric trace gases over Dhaka, Bangladesh, *J. Atmos. Chem.*, 81, 4, <https://doi.org/10.1007/s10874-024-09457-y>, 2024.
- Kim, M.-K., Park, D., Kim, M., Heo, J., Park, S., and Chong, H.: A study on characteristic emission factors of exhaust gas from diesel locomotives, *Int. J. Environ. Res. Public Health*, 17, 3788, <https://doi.org/10.3390/ijerph17113788>, 2020.
- 675 Kondo, Y., Komazaki, Y., Miyazaki, Y., Moteki, N., Takegawa, N., Kodama, D., Deguchi, S., Nogami, M., Fukuda, M., Miyakawa, T., Morino, Y., Koike, M., Sakurai, H., and Ehara, K.: Temporal variations of elemental carbon in Tokyo, *J. Geophys. Res.: Atmos.*, 111, <https://doi.org/10.1029/2005JD006257>, 2006.
- Lelieveld, J., Gromov, S., Pozzer, A., and Taraborrelli, D.: Global tropospheric hydroxyl distribution, budget and reactivity, *Atmos. Chem. Phys.*, 16, 12477–12493, <https://doi.org/10.5194/acp-16-12477-2016>, 2016.
- 680 Levin, I., Kromer, B., Schmidt, M., and Sartorius, H.: A novel approach for independent budgeting of fossil fuel CO₂ over Europe by ¹⁴CO₂ observations, *Geophys. Res. Lett.*, 30, <https://doi.org/10.1029/2003GL018477>, 2003.
- Li, Y., Deng, J., Mu, C., Xing, Z., and Du, K.: Vertical distribution of CO₂ in the atmospheric boundary layer: Characteristics and impact of meteorological variables, *Atmos. Environ.*, 91, 110–117, <https://doi.org/10.1016/j.atmosenv.2014.03.067>, 2014.
- 685 Li, Y., Tong, H., Zhuo, Y., Chen, C., and Xu, X.: Simultaneous removal of SO₂ and trace SeO₂ from flue gas: Effect of product layer on mass transfer, *Environ. Sci. Technol.*, 40, 4306–4311, <https://doi.org/10.1021/es052381s>, 2006.

- Li, Y., Ma, Z., Han, T., Quan, W., Wang, J., Zhou, H., He, D., and Dong, F.: Long-term declining in carbon monoxide (CO) at a rural site of Beijing during 2006–2018 implies the improved combustion efficiency and effective emission control, *J. Environ. Sci.*, 115, 432–442, <https://doi.org/10.1016/j.jes.2020.11.011>, 2022.
- 690 Lin, J., Fang, S., He, R., Tang, Q., Qu, F., Wang, B., and Xu, W.: Monitoring ocean currents during the passage of Typhoon Muifa using optical-fiber distributed acoustic sensing, *Nat. Commun.*, 15, 1111, <https://doi.org/10.1038/s41467-024-45412-x>, 2024.
- Lin, Y., Zhang, Y., Xie, F., Fan, M., and Liu, X.: Substantial decreases of light absorption, concentrations and relative contributions of fossil fuel to light-absorbing carbonaceous aerosols attributed to the COVID-19 lockdown in east China, *Environ. Pollut.*, 275, 116615, <https://doi.org/10.1016/j.envpol.2021.116615>, 2021.
- 695 Lin, Y., Li, S., Yu, Y., Lu, M., Chen, B., Chen, Y., Zang, K., Liu, S., Qi, B., and Fang, S.: A new regional background atmospheric station in the Yangtze River Delta region for carbon monoxide: Assessment of spatiotemporal characteristics and regional significance, *Atmosphere*, 16, <https://doi.org/10.3390/atmos16010101>, 2025.
- 700 Liu, L., Tans, P. P., Xia, L., Zhou, L., and Zhang, F.: Analysis of patterns in the concentrations of atmospheric greenhouse gases measured in two typical urban clusters in China, *Atmos. Environ.*, 173, 343–354, <https://doi.org/10.1016/j.atmosenv.2017.11.023>, 2018.
- Liu, P., Zhang, C., Mu, Y., Liu, C., Xue, C., Ye, C., Liu, J., Zhang, Y., and Zhang, H.: The possible contribution of the periodic emissions from farmers' activities in the North China Plain to atmospheric water-soluble ions in Beijing, *Atmos. Chem. Phys.*, 16, 10097–10109, <https://doi.org/10.5194/acp-16-10097-2016>, 2016.
- 705 Liu, S., Fang, S., Liang, M., Ma, Q., and Feng, Z.: Study on CO data filtering approaches based on observations at two background stations in China, *Sci. Total Environ.*, 691, 675–684, <https://doi.org/10.1016/j.scitotenv.2019.07.162>, 2019.
- Liu, S., Chen, B., Fang, S., Zhang, C., Zang, K., He, W., Chen, Y., Lin, Y., Jin, Z., Chen, Z., Lan, W., and Xu, H.: Contrasting high-resolution vertical CO₂ patterns: Insights from economically developed regions in Southeast China, *J. Geophys. Res.: Atmos.*, 130, <https://doi.org/10.1029/2024jd043181>, 2025.
- 710 Meng, F., Hu, H., Sun, Y., Zhang, L., Hou, J., Zhang, Z., Pang, L., Cai, B., and Shan, Y.: Full-scope carbon dioxide emission dataset for Chinese cities in 2023, *Sci. Data*, 12, 1672, <https://doi.org/10.1038/s41597-025-05949-y>, 2025.
- MOT: The Ministry of Transport of the People's Republic of China—Statistical Report on Transportation Industry Development 2022, available at: https://xxgk.mot.gov.cn/2020/jigou/zhghs/202205/t20220517_3655699.html (last access: 3 August 2025), 2022.
- 715 NOAA, Air Resources Laboratory: Global data assimilation system (GDAS) model one - degree data [data set], <https://www.ready.noaa.gov/archives.php>, 2024.
- Oke, T. R.: The distinction between canopy and boundary-layer urban heat islands, *Atmosphere*, 14, 268–277, <https://doi.org/10.1080/00046973.1976.9648422>, 1976.
- 720 Patel, A., Mallik, C., Chandra, N., Patra, P. K., and Steinbacher, M.: Revisiting regional and seasonal variations in decadal carbon monoxide variability: Global reversal of growth rate, *Sci. Total Environ.*, 909, 168476, <https://doi.org/10.1016/j.scitotenv.2023.168476>, 2024.
- Paul, S., Ghosh, S., Mathew, M., Devanand, A., Karmakar, S., and Niyogi, D.: Increased spatial variability and intensification of extreme monsoon rainfall due to urbanization, *Sci. Rep.*, 8, 3918, <https://doi.org/10.1038/s41598-018-22322-9>, 2018.
- 725 Polissar, A. V., Hopke, P. K., Paatero, P., Kaufmann, Y. J., Hall, D. K., Bodhaine, B. A., Dutton, E. G., and Harris, J. M.: The aerosol at Barrow, Alaska: long-term trends and source locations, *Atmos. Environ.*, 33, 2441–2458, [https://doi.org/10.1016/S1352-2310\(98\)00423-3](https://doi.org/10.1016/S1352-2310(98)00423-3), 1999.

- 730 Popa, M. E., Vollmer, M. K., Jordan, A., Brand, W. A., Pathirana, S. L., Rothe, M., and Röckmann, T.: Vehicle emissions of greenhouse gases and related tracers from a tunnel study: CO : CO₂, N₂O : CO₂, CH₄ : CO₂, O₂ : CO₂ ratios, and the stable isotopes ¹³C and ¹⁸O in CO₂ and CO, *Atmos. Chem. Phys.*, 14, 2105–2123, <https://doi.org/10.5194/acp-14-2105-2014>, 2014.
- Pu, J., Xu, H., He, J., Fang, S., and Zhou, L.: Estimation of regional background concentration of CO₂ at Lin'an Station in Yangtze River Delta, China, *Atmos. Environ.*, 94, 402–408, <https://doi.org/10.1016/j.atmosenv.2014.05.060>, 2014.
- 735 Rogelj, J., McCollum, D. L., Reisinger, A., Meinshausen, M., and Riahi, K.: Probabilistic cost estimates for climate change mitigation, *Nature*, 493, 79–83, <https://doi.org/10.1038/nature11787>, 2013.
- Rousseau, D.-D., Duzer, D., Etienne, J.-L., Cambon, G., Jolly, D., Ferrier, J., and Schevin, P.: Pollen record of rapidly changing air trajectories to the North Pole, *J. Geophys. Res.: Atmos.*, 109, <https://doi.org/10.1029/2003JD003985>, 2004.
- Ruckstuhl, A. F., Henne, S., Reimann, S., Steinbacher, M., Vollmer, M. K., O'Doherty, S., Buchmann, B., and Hueglin, C.: Robust extraction of baseline signal of atmospheric trace species using local regression, *Atmos. Meas. Tech.*, 5, 2613–740 2624, <https://doi.org/10.5194/amt-5-2613-2012>, 2012.
- Seiler, W.: Cycle of atmospheric CO, *Tellus*, 26, 116–135, <https://doi.org/10.1111/j.2153-3490.1974.tb01958.x>, 2010.
- Seinfeld, J. H. and Pandis, S. N.: *Atmospheric chemistry and physics: From air pollution to climate change* (2nd ed.), John Wiley & Sons, <https://doi.org/10.1063/1.882420>, 2016.
- 745 SHMS: Shanghai Municipal Human Resources and Social Security Bureau, available at: http://rsj.sh.gov.cn/tgwyrshb_17088/20211220/t0035_1404512.html (last access: 11 January 2024), 2022.
- Super, I., Denier van der Gon, H. A. C., Visschedijk, A. J. H., Moerman, M. M., Chen, H., van der Molen, M. K., and Peters, W.: Interpreting continuous in-situ observations of carbon dioxide and carbon monoxide in the urban port area of Rotterdam, *Atmos. Pollut. Res.*, 8, 174–187, <https://doi.org/10.1016/j.apr.2016.08.008>, 2017.
- 750 Thoning, K. W., Tans, P. P., and Komhyr, W. D.: Atmospheric carbon dioxide at Mauna Loa Observatory: 2. Analysis of the NOAA GMCC data, 1974–1985, *J. Geophys. Res.: Atmos.*, 94, 8549–8565, <https://doi.org/10.1029/JD094iD06p08549>, 1989.
- Tian, X., Ren, B., Xie, P., Xu, J., Li, A., Hu, F., Zheng, J., Ren, H., Hu, Z., Pan, Y., Huang, X., Zhang, Z., Lv, Y., Tian, W., and Wang, Z.: The vertical distribution and potential sources of aerosols in the Yangtze River Delta region of China during open straw burning, *Sci. Total Environ.*, 849, 157749, <https://doi.org/10.1016/j.scitotenv.2022.157749>, 2022.
- 755 Tohjima, Y., Kubo, M., Minejima, C., Mukai, H., Tanimoto, H., Ganshin, A., Maksyutov, S., Katsumata, K., Machida, T., and Kita, K.: Temporal changes in the emissions of CH₄ and CO from China estimated from CH₄/CO₂ and CO/CO₂ correlations observed at Hateruma Island, *Atmos. Chem. Phys.*, 14, 1663–1677, <https://doi.org/10.5194/acp-14-1663-2014>, 2014.
- 760 Tong, K., Fang, A., Li, Y., Shi, L., Wang, Y., Wang, S., and Ramaswami, A.: The collective contribution of Chinese cities to territorial and electricity-related CO₂ emissions, *J. Cleaner Prod.*, 189, 910–921, <https://doi.org/10.1016/j.jclepro.2018.04.037>, 2018.
- Tsutsumi, Y., Mori, K., Ikegami, M., Tashiro, T., and Tsuboi, K.: Long-term trends of greenhouse gases in regional and background events observed during 1998–2004 at Yonagunijima located to the east of the Asian continent, *Atmos. Environ.*, 40, 5868–5879, <https://doi.org/10.1016/j.atmosenv.2006.04.036>, 2006.
- 765 Vásquez, M., Lara, W., Valle, J. I. D., and Sierra, C.: Reconstructing past fossil-fuel CO₂ concentrations using tree rings and radiocarbon in the urban area of Medellín, Colombia, *Environ. Res. Lett.*, 17, 055008, <https://doi.org/10.1088/1748-9326/ac63d4>, 2022.

- Vega, M., Cespedes, L., Lombardo, F., Re, G., Garcia, N., Busnelli, A., Fedele, F. D., Lopez, M., Pomar, J., Salvati, A., and Piacentini, R.: Measurements and modelization of the Rosario City Heat Island, Argentina - Preliminary Results, IOP Conf. Ser.: Mater. Sci. Eng., 471, 092088, <https://doi.org/10.1088/1757-899X/471/9/092088>, 2019.
- 770 Wang, L., Li, D., Gao, Z., Sun, T., Guo, X., and Bou-Zeid, E.: Turbulent transport of momentum and scalars above an urban canopy, *Boundary Layer Meteorol.*, 150, 485–511, <https://doi.org/10.1007/s10546-013-9877-z>, 2014.
- Wang, L., Gu, X., Slater, L. J., Lai, Y., Zhang, X., Kong, D., Liu, J., and Li, J.: Indirect and direct impacts of typhoon In-Fa (2021) on heavy precipitation in inland and coastal areas of China: Synoptic-scale environments and return period analysis, *Mon. Weather Rev.*, 151, 2377–2395, <https://doi.org/10.1175/MWR-D-22-0241.1>, 2023.
- 775 Wang, L., Xiong, Q., Wu, G., Gautam, A., Jiang, J., Liu, S., Zhao, W., and Guan, H.: Spatio-temporal variation characteristics of PM_{2.5} in the Beijing–Tianjin–Hebei Region, China, from 2013 to 2018, *Int. J. Environ. Res. Public Health*, 16, 4276, <https://doi.org/doi:10.3390/ijerph16214276>, 2019.
- Wang, S., Wang, Q., Zhu, S., Zhou, M., Qiao, L., Huang, D., Ma, Y., Lu, Y., Huang, C., Fu, Q., Duan, Y., and Yu, J. Z.: Hourly organic tracers-based source apportionment of PM_{2.5} before and during the Covid-19 lockdown in suburban Shanghai, China: Insights into regional transport influences and response to urban emission reductions, *Atmos. Environ.*, 289, 119308, <https://doi.org/10.1016/j.atmosenv.2022.119308>, 2022.
- 780 Wang, Y., Munger, J. W., Xu, S., McElroy, M. B., Hao, J., Nielsen, C. P., and Ma, H.: CO₂ and its correlation with CO at a rural site near Beijing: implications for combustion efficiency in China, *Atmos. Chem. Phys.*, 10, 8881–8897, <https://doi.org/10.5194/acp-10-8881-2010>, 2010.
- 785 Wang, Z., Li, J., Wang, X., Pochanart, P., and Akimoto, H.: Modeling of regional high ozone episode observed at two mountain sites (Mt. Tai and Huang) in East China, *J. Atmos. Chem.*, 55, 253–272, <https://doi.org/10.1007/s10874-006-9038-6>, 2006.
- WDCGG: WMO WDCGG Data Summary reports No. 49, available at: <https://gaw.kishou.go.jp/static/publications/summary/sum49/sum49.pdf> (last access: 20 November 2025), 2025a.
- 790 WDCGG, World Data Centre for Greenhouse Gases: Greenhouse Gases Data [data set], <https://gaw.kishou.go.jp/search>, 2025b.
- Westerdahl, D., Wang, X., Pan, X., and Zhang, K. M.: Characterization of on-road vehicle emission factors and microenvironmental air quality in Beijing, China, *Atmos. Environ.*, 43, 697–705, <https://doi.org/10.1016/j.atmosenv.2008.09.042>, 2009.
- 795 Winderlich, J., Gerbig, C., Kolle, O., and Heimann, M.: Inferences from CO₂ and CH₄ concentration profiles at the Zotino Tall Tower Observatory (ZOTTO) on regional summertime ecosystem fluxes, *Biogeosciences*, 11, 2055–2068, <https://doi.org/10.5194/bg-11-2055-2014>, 2014.
- WMO: WMO Greenhouse Gas Bulletin. No. 21. The State of Greenhouse Gases in the Atmosphere Based on Global Observations through 2024, available at: <https://library.wmo.int/records/item/69654-no-21-16-october-2025> (last access: 27 October 2025), 2025.
- 800 Wu, D., Liu, J., Wennberg, P. O., Palmer, P. I., Nelson, R. R., Kiel, M., and Eldering, A.: Towards sector-based attribution using intra-city variations in satellite-based emission ratios between CO₂ and CO, *Atmos. Chem. Phys.*, 22, 14547–14570, <https://doi.org/10.5194/acp-22-14547-2022>, 2022.
- Xia, L., Zhang, G., Liu, L., Li, B., Zhan, M., Kong, P., and Wang, H.: Atmospheric CO₂ and CO at Jingdezhen station in central China: Understanding the regional transport and combustion efficiency, *Atmos. Environ.*, 222, 117104, <https://doi.org/10.1016/j.atmosenv.2019.117104>, 2020.
- 805

- Xiong, H., Fang, S., Zang, K., Lin, Y., Qiu, S., Hong, H., Li, J., Qing, X., and Jiang, K.: The utility model relates to a gas pretreatment device, CN215876659U. 2022-02-22, <http://epub.cnipa.gov.cn/Dxb/PatentDetail>, 2022.
- 810 Yang, Y., Zhou, M., Wang, T., Yao, B., Han, P., Ji, D., Zhou, W., Sun, Y., Wang, G., and Wang, P.: Spatial and temporal variations of CO₂ mole fractions observed at Beijing, Xianghe, and Xinglong in North China, *Atmos. Chem. Phys.*, 21, 11741–11757, <https://doi.org/10.5194/acp-21-11741-2021>, 2021.
- 815 Yang, Y., Zhou, M., Langerock, B., Sha, M. K., Hermans, C., Wang, T., Ji, D., Vigouroux, C., Kumps, N., Wang, G., De Mazière, M., and Wang, P.: New ground-based Fourier-transform near-infrared solar absorption measurements of XCO₂, XCH₄ and XCO at Xianghe, China, *Earth Syst. Sci. Data*, 12, 1679–1696, <https://doi.org/10.5194/essd-12-1679-2020>, 2020.
- Ye, C., Zhou, X., Zhang, Y., Wang, Y., Wang, J., Zhang, C., Woodward-Massey, R., Cantrell, C., Mauldin, R. L., Campos, T., Hornbrook, R. S., Ortega, J., Apel, E. C., Haggerty, J., Hall, S., Ullmann, K., Weinheimer, A., Stutz, J., Karl, T., Smith, J. N., Guenther, A., and Song, S.: Synthesizing evidence for the external cycling of NO_x in high- to low-NO_x atmospheres, *Nat. Commun.*, 14, 7995, <https://doi.org/10.1038/s41467-023-43866-z>, 2023.
- 820 Ye, J., Zhang, Y., Yao, W., Liu, H., Lei, S., Zhang, Y., Zhang, J., Li, S., Lv, S., Wu, L., Tang, X., Sun, Y., Xin, J., Li, J., Wang, Z., Liu, L., Su, H., and Pan, X.: Significant shift of footprint patterns and pollutant source contributions: insights from observations at Shanghuang observatory, East China, *Environ. Res. Lett.*, 19, <https://doi.org/10.1088/1748-9326/ad8369>, 2024.
- 825 Yuan, Y., Ries, L., Petermeier, H., Steinbacher, M., Gómez-Peláez, A. J., Leuenberger, M. C., Schumacher, M., Trickl, T., Couret, C., Meinhardt, F., and Menzel, A.: Adaptive selection of diurnal minimum variation: a statistical strategy to obtain representative atmospheric CO₂ data and its application to European elevated mountain stations, *Atmos. Meas. Tech.*, 11, 1501–1514, <https://doi.org/10.5194/amt-11-1501-2018>, 2018.
- Zhang, F., Chen, Y., Tian, C., Lou, D., Li, J., Zhang, G., and Matthias, V.: Emission factors for gaseous and particulate pollutants from offshore diesel engine vessels in China, *Atmos. Chem. Phys.*, 16, 6319–6334, <https://doi.org/10.5194/acp-16-6319-2016>, 2016.
- 830 Zhang, P., Wang, Y., Chen, T., Yu, Y., Ma, Q., Liu, C., Li, H., Chu, B., and He, H.: Insight into the Mechanism and Kinetics of the Heterogeneous Reaction between SO₂ and NO₂ on Diesel Black Carbon under Light Irradiation, *Environ. Sci. Technol.*, 57, 17718–17726, <https://doi.org/10.1021/acs.est.2c09674>, 2023.
- 835 Zhang, W., Tong, S., Jia, C., Ge, M., Ji, D., Zhang, C., Liu, P., Zhao, X., Mu, Y., Hu, B., Wang, L., Tang, G., Li, X., Li, W., and Wang, Z.: Effect of different combustion processes on atmospheric nitrous acid formation mechanisms: a winter comparative observation in urban, suburban and rural areas of the North China Plain, *Environ. Sci. Technol.*, 56, 4828–4837, <http://doi.org/10.1021/acs.est.1c07784>, 2022.
- 840 Zhao, D., Xin, J., Wang, W., Jia, D., Wang, Z., Xiao, H., Liu, C., Zhou, J., Tong, L., Ma, Y., Wen, T., Wu, F., and Wang, L.: Effects of the sea-land breeze on coastal ozone pollution in the Yangtze River Delta, China, *Sci. Total Environ.*, 807, 150306, <https://doi.org/10.1016/j.scitotenv.2021.150306>, 2022.
- Zhao, J., Chen, H., Qi, X., Chi, X., Jia, M., Jiang, F., Zhong, S., Zheng, B., and Ding, A.: Observed decade-long improvement of combustion efficiency in the Yangtze River Delta region in China, *Environ. Res. Lett.*, 19, 074001, <https://doi.org/10.1088/1748-9326/ad521e>, 2024.
- 845 Zhao, X., Ding, J. M., and Suna, H. H.: Structural Design of Shanghai Tower for wind Loads, *Procedia Eng.*, 14, 1759–1767, <https://doi.org/10.1016/j.proeng.2011.07.221>, 2011.

Zheng, B., Chevallier, F., Yin, Y., Ciais, P., Fortems-Cheiney, A., Deeter, M. N., Parker, R. J., Wang, Y., Worden, H. M., and Zhao, Y.: Global atmospheric carbon monoxide budget 2000–2017 inferred from multi-species atmospheric inversions, *Earth Syst. Sci. Data*, 11, 1411–1436, <https://doi.org/10.5194/essd-11-1411-2019>, 2019.

850 Zhu, W., Kattel, S., Jiao, F., and Chen, J. G.: Shape-controlled CO₂ electrochemical reduction on nanosized Pd hydride cubes and octahedra, *Adv. Energy Mater.*, 9, <https://doi.org/10.1002/aenm.201802840>, 2019.